Flávia Cristina Monteiro Rocha

Licenciada em Ciências de Engenharia Física

Electrical characterization and modification of low dimensional oxide semiconductors for sensor applications

Dissertação para obtenção do Grau de Mestre em Engenharia Física

Orientadores: Prof. Doctor Ana Gomes Silva, FCT-UNL

Doctor Katharina Lorenz, IPFN, IST-UL

Júri:

Presidente: Prof. Doctor Isabel Catarino, FCT-UNL

Arguentes: Prof. Doctor João Cruz, FCT-UNL

Vogais: Doctor Katharina Lorenz, IPFN, IST-UL

FACULDADE DE CIÊNCIAS E TECNOLOGIA
UNIVERSIDADE NOVA DE LISBOA

November, 2015

Acknowledgments

The realization of this Theses allowed me to fulfill two childhood dreams this year: ending my Master in Physics Engineering and work at CTN.

For this, and for all the path until now, I would like to thank all of those who helped me to get here.

To Dr. Katharina Lorenz, who allowed me to be part of her incredible research team in CTN and be part of a true research project in physics. Thank you for allowing me to have all the time and freedom to experiment and ease my constant thirst of knowledge. But most of all, thank you for all of the good personal lessons: passion and dedication, along with a kindness, compassion and undying faith in all of those around her, making us want to do nothing but the best to make her proud. Thank you for your patience and understanding in the final step of the thesis.

To Prof. Dr. Ana G. Silva, my most heartfelt and big thank you. Not only for all the long and late hours of discussions, of teaching me, of sharing the most unbelievable amount of knowledge about everything and anything, but most of all, for the kindness that helped me in the most difficult of times, for listening and truly caring, without ever questioning. Thank you, from the bottom of my heart, for all the good professional, but much more important, personal orientation.

To Dr. Bianchi Méndez, Dr. Emilio Nogales, Dr. Maria Vila Santos and Dr.Carlos Viejo from Dpto. Física de Materiales, da Universidad Complutense de Madrid, Spain and Encarna Villora and Kiyoshi Shimamura from the National Institute for Materials Science, Japan, for all the samples that allowed this work to be done and also for the great amount of them, since I tend to finish all off the stock available.

I would also like to thank to all the IPFN group, I still can't believe how nice everyone is and how great and familiar the group is. To Dr. Eduardo Alves that keeps on taking care and motivating all the groups to do a good job always with good energy. To my team and cabinet partners, Marco Peres and Miguel Sequeira, for the incredible long hours of physical discussion and for liking it. Thank you Marco for all the knowledge that you shared and for caring. Thank you Miguel for always share with such great enthusiasm everything you know and for the long quantum talks. I will never know how you are able to stock so much information, with such accuracy in your head. Thank you Sérgio Magalhães, Djibril Faye for all the meetings and patience to hear my presentations. To Luis Alves, for the incredible resilience and patience, always with the most ge-

niality and making those incredible long beam days the best ones, even if you seem to disturb all the electronics around you. To Luis Ferreira, Carlos Cruz, Filomena, Jorge and Dª Vitória for making me feel home since day one. Also for all the good principles and showing that is possible to be a great professional and be a great college at the same time. I don't think that CTN could survive without you.

To all my colleges. It's amazing how many great people I have had the pleasure to meet along these years. I wish you all the best and thank you for making everything more fun.

I want to give a really special and warm thank you to Marta e Francisco. I can say now that I will leave college richer for I have had the pleasure of working with you and most important, be your friend. I still can't believe the long nights of support, fun and laugher that we shared. Yes, I think we share a brain. And I adore you.

To Andreia, Cristina and Cristiana. You are always in my heart. To Evaldo for always showing what friendship is made off. You are the meaning behind the word. This would not be possible without Caderno Diário days. For all the good advice and long talks, the friendship, the fun and helping me whenever I needed it, I want to thank Raquel Coutinho, Susana Sério and Dina Capelo. With you I had the most fun days.

To Dª Zé and Sr. Carlos, for always taking so good care of me, for all the great hours that we shared, the card games and for your kindness.

To my Mom, for she is the reason why I always believed I could follow my dreams. This was your great lesson to me, you made me believe that all dreams are possible, that I could do anything. You never believe that the world is too small. Thank you for all the strength and fight. Thank you mom from my heart.

To the most important person in my life. To my half, my soulmate, my love, André Varelas. I genuinely don't think that I would have made it without you. You are the reason behind all of this. You believe in me before all, you gave me strength, you were always there. With you, life became the dream. I'm the most fortunate person in the world because I have you. It was the most fulfilling experience to achieve my dream side by side with you. Thank you for your Love.

This work was achieved thanks to the funding of the projects PTDC/CTM-NAN/2156/2012 and PTDC/FIS- NAN/0973/2012, by national funds from FCT.

Abstract

This work reviews the recent research on ion and UV irradiation of β-Ga_2O_3 and α-MoO_3 crystal structures. These crystalline materials belong to the transparent conductive oxides (TCOs) family due to their wide energy band gap and their transparency for visible light. In-situ Electrical Characterization (EC) during proton and UV irradiation of the samples was carried out. Conductivity changes observed under ion and UV irradiation, designated respectively by Ion-Conductivity (IC) and Photoconductivity (PC), were measured and compared. Persistent conductivity phenomena were observed and analyzed. For the electrical characterization, a recently acquired Parametric Analyzer was used and tested for the first time. A new home-built chamber for the EC, combined with other techniques such as Rutherford Backscattering Spectrometry (RBS), Particle-Induced X-Ray Emission (PIXE) and Ion-Luminescence (IL) was tested. Different crystal thicknesses were produced by crystal exfoliation using the scotch-tape technique, which was proved in this work, to be an inexpensive and efficient technique to obtained samples with surfaces free of contamination. In order to perform the in-situ experiments, electrical contacts were produced and tested.

Keywords: Gallium Oxide; Molybdenum Oxide; Electrical Contacts; Persistent Ion conductivity; Persistent Photoconductivity.

Resumo

Este trabalho vem na continuidade de trabalhos recentes sobre irradiação iónica e de UV em estruturas cristalinas de β-Ga_2O_3 e α-MoO_3.

Estes materiais cristalinos pertencem à família dos óxidos condutores transparentes (*TCOs*) devido ao seu largo hiato de energia e transparência à radiação no visível. Foi realizada Caracterização Elétrica (EC), *in-situ*, durante irradiação iónica e com UV. As alterações observadas para a fotocondutivade (PC), devido à irradiação UV, e para a iono-condutividade (IC), devido à irradiação com iões, foram analisadas e comparadas. Como resultado de ambos os tipos de irradiação, foi observado e analisado o fenómeno de condutividade persistente. Para a caraterização elétrica, foi usado e testado pela primeira vez, um analisador paramétrico recentemente adquirido pelo grupo. Foi testado um novo sistema experimental, projetado e construído no próprio laboratório para a caracterização elétrica *in-situ* em simultâneo com outras técnicas de caracterização que são Espetrometria de Retrodispersão de Rutherford (RBS), Emissão de Raios-X Induzida por Partículas (PIXE) e Iono-Luminescência (IL). Cristais de diferentes espessuras foram produzidos através de exfoliação mecânica utilizando a técnica da fita-cola, que provou ser eficiente e económico para a obtenção de amostras finas e livres de contaminação. Foram realizados contactos elétricos para a caracterização *in-situ*.

Palavras-chave: Óxido de Gálio; Óxido de Molibdénio; Contactos Elétricos; Ionocondutividade Persistente; Fotoconductividade Persistente.

Contents

List of figures

List of tables

List of abbreviations

UV	Ultraviolet
Ga_2O_3	Gallium Oxide
MoO_3	Molybdenum Trioxide
TCOs	Transparent Conductive Oxides
EC	Electrical Characterization
IC	Iono-Conductivity
PC	Photoconductivity
RBS	Rutherford Backscattering Spectrometry
PIXE	Particle-Induced X-Ray Emission
Il	Ion-Luminescence
Si	Silicon
GaAs	Gallium Arsenide
GaN	Gallium Nitride
2D	Two Dimensional
MSM	Metal-Semiconductor-Metal
Ga	Gallium
O	Oxygen
STM	Scanning Tunneling Microscope
SnO_2	Tin Dioxide
VLS	Vapor-Liquid-Solid

HRTEM	High Resolution Transmission Electron Microscopy
VS	Vapor-Solid
Mo	Molybdenum
SEM	Scanning Electron Microscope

1

Introduction

1.1 Motivation

Semiconductors exhibit a wide spectrum of phenomena, in terms of electrical conductivity or in terms of optical effects. They have been studied since 1920's and in 1940 the first transistor was invented by Shockley, Bardeen and Brattain [1]. Since then, technology has undergone a great development and our daily life is nowadays unthinkable without microelectronics present in televisions, mobile phones, personal computers etc. In addition to conventional semiconductors such as Si and GaAs, in the last decades the interest in more complex semiconductor families such as nitrides (e.g. GaN) and metal-oxides has been rising [2]. Furthermore, nanostructures such as nanowires or ultrathin systems are expected to contribute to the miniaturization of electronics devices as well as to the development of novel applications.

One of the interesting characteristics of low dimensional crystal structures is related with their dimensional limit leading to different atomic confinement conditions in space. Furthermore, their large aspect ratios lead to high surface area to volume ratios increasing effects related to the semiconductor surface. In the case of 2D materials, different types of forces act between atoms of adjacent planes and between atoms belonging to the same plane, the latter being much stronger than the former allowing the easy production of ultrathin systems.

1.2 Main Goals

The main purpose of this work was to study the electrical properties, such as photoconductivity and ion-conductivity, of low dimensional semiconductor oxides and evaluate their response as radiation sensors under UV and proton irradiation.

The first task to be carried out in this thesis was the production and optimization of the electrical junctions for the materials in study, i.e. gallium oxide and molybdenum oxide. In fact, this was a challenging task. Due to the bandgap characteristics of these oxides (wide bandgap) and their irregular shape at nanoscale, junctions of different shape and arrangement need to be implemented. In fact, current-voltage curves of devices built with the same metallic contacts and produced under the same conditions can present different behaviors, showing ohmic to Schottky characteristics. These different results are attributed to interfacial chemistry and natural surface disorder [3]. Electrical junction properties need to be thoroughly understood in order to allow the currents (often in the nano-Ampère range) to be measured with low noise and avoiding misinterpretation of physical phenomena that can occur during the measurements [4].

A recently acquired parametric analyzer, for electrical characterization, had to be tested. In addition, a new irradiation chamber allowing in-situ electrical characterization during UV and high energetic protons irradiation, was developed and tested. The interest in such studies is twofold. As published in previous works [5], it is known that changing the crystalline structure, by controlled formation of defects, will change electrical and optical proprieties. On the one hand, such defect engineering may in fact be exploited for applications in sensors for radiation detectors. On the other hand, and on more fundamental grounds, this measurements contribute to the assessment of this materials for future radiation resistant electronics. Understanding the effect of radiation defects on electrical properties is extremely important for future doping studies using ion implantation. Therefore the final objective of this work was the investigation of the electrical properties of the aforementioned materials and how these properties change during UV and proton irradiation.

2

State of the art

Semiconductor nanostructures are interesting materials for many applications such as electromagnetic radiation sensors, particle interaction sensors, gas sensors, nano-electronics and nano-light emitters in nanoscale dimension devices [6]. Because of their electronic structure, with well-defined band gap, defect centers that appear in the crystal structure will cause energy levels to appear in the forbidden band gap. These energy levels or traps, may significantly influence the conductivity of the electric device, since they influence the recombination mechanisms of free electrons and holes. Evaluating the electronic behavior of the device at the same time that irradiation processes are taking place will allow the study of the effects caused by ionization and defect formation processes induced by the irradiation. These studies can also be a good basis for further studies on ion implantation [7].

Semiconductor oxides have a large band gap and such characteristic provides a good base for optical transparency for electronic devices. This characteristic could induce to think that these materials are inapt for electronic conduction. However, they are proved to be good conductors and since they continue to be transparent to visible light this new class of materials is designated by Transparent Conductive Oxide semiconductors (TCOs), as reported by Hosono [8].

Also, some semiconductor oxides, such as thin crystalline films of MoO_3 and Ga_2O_3, are considered to be in a sense 2D materials due to the nature of the forces established between adjacent crystal planes which are of Van der Waals type.

According to Feynman[9], Van der Waals' forces arise from the fact that the electron charge distribution is not isotropic around the nuclei, when in a molecular structure, being higher between two adjacent nuclei. This anisotropic charge distribution creates a dipolar moment proportional to $(1\backslash R^7)$ where R is the distance between the negative charge and the nucleus, which is large compared to the atomic radii of isolated at-

oms. An attractive force arises between such anisotropic molecules due to the Coulomb forces between the negative electron cloud of one molecule and the positive side of another molecule. The same considerations are made about covalent bonds but for distances R in the order of the atomic radii, which reflects a dipolar moment proportional to 1/R, leading to much stronger forces than for the Van der Waals case.

Due to the forces established between adjacent crystalline planes being Van der Waals in opposition to the covalent bonds made between atoms from the same plane, these materials are easily exfoliated, like in graphene, the most famous case of such materials since 2010 when the Physics Nobel Prize was awarded for the development of a one monolayer graphene device produced by mechanical exfoliation using scotch tape [10].

In order to functionalize the semiconductors, Metal-Semiconductor-Metal (MSM) devices were made. MSM photodetectors have been studied and shown to be faster than photodiodes. It has been reported that they also have a wider wavelength sensitivity, some reaching hundreds of gigahertz [11].

In this work, the main focus was on Ga_2O_3 and MoO_3 single crystals. These materials both present a persistent conductivity after both UV and particle exposure. A two-step relaxation can be observed for both materials when the excitation is switched off, where a sharp drop takes place followed by a slow decline, as reported for other studied materials, such as Zinc Oxide [6].

3

Oxide Semiconductors Studied

The crystals studied in the present work were produced by other groups. Exfoliated samples were obtained by our group.

There are many studies made about metal oxide thins films, but not as much as about single crystals oxides, where the most existing studies are about zinc oxide and titanium oxide [12].

3.1 **Gallium oxide**

The material is both conducting and transparent and this is an extremely important feature for future electronic devices [13].

β-Ga_2O_3 has the largest band gap (between 4.8 and 4.9 eV), that corresponds to 253-258 nm, of all Transparent Conductive Oxide (TCO), which means that it is transparent in the visible and UV wavelength region [14].

The beta phase is the most stable form of gallium oxide, with a monoclinic base centered crystal structure (see Fig. 3.1), where Ga has different coordination numbers with tetrahedral and octahedral symmetry, while O resides at the corners of these tetrahedral and octahedral.

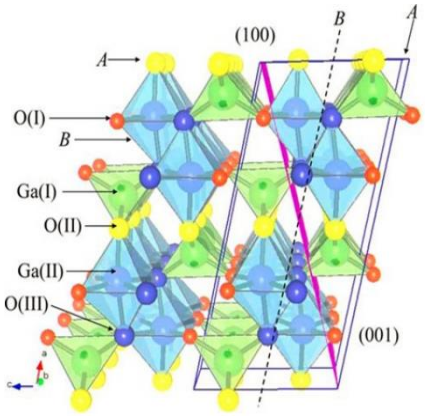

Figure 3.1 - Crystal Structure of Gallium Oxide [15]

The gallium flakes studied were taken and then exfoliated from the gallium bulk single crystals samples (Fig. 3.2), grown using the floating zone technique in Japan, with 99.99% purity gallium oxide powders, by a set-up equipped with four halogen lamps and the corresponding ellipsoidal mirrors and were cleaved on the (100) plane [16].

The float zone crystal growth, pioneered by Samsung AG, produces highly pure single crystals using melt of a material and growing single crystals oriented by a seed that is in the center of the melt. The melt is pushed along the seed by swirling the seed at a constant speed. It is a technique appropriate for growing crystals with diameters lower than 150 nm, because it needs surface tension to be strong enough to keep the liquid in place around the seed.

Because this procedure is done in vacuum or in an ambience of inert gases, the crystals produced have high purity [17].

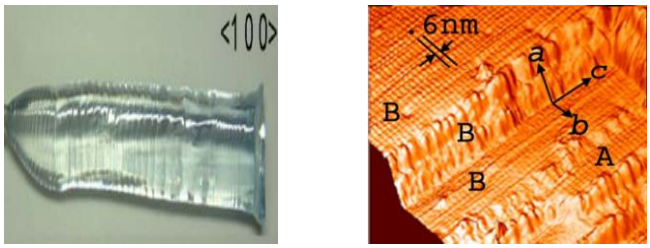

Figure 3.2 - Left: picture of beta Gallium oxide [16] Right: Scanning Tunneling Microscopy (STM) image of Gallium oxide (100) surface [12].

The STM image (see Fig. 3.2), reveals the parallel rows along the band c axis, where A and B represent terraces of the sample surface where each step has half width of the unit cell, because a axis is not perpendicular to the surface [12].

The gallium oxide nanowires (Fig. 3.3) were grown and doped with tin by the group of *Departamento de Física de Materiales at Universidad Complutense De Madrid, Facultad De Ciencias Físicas*.

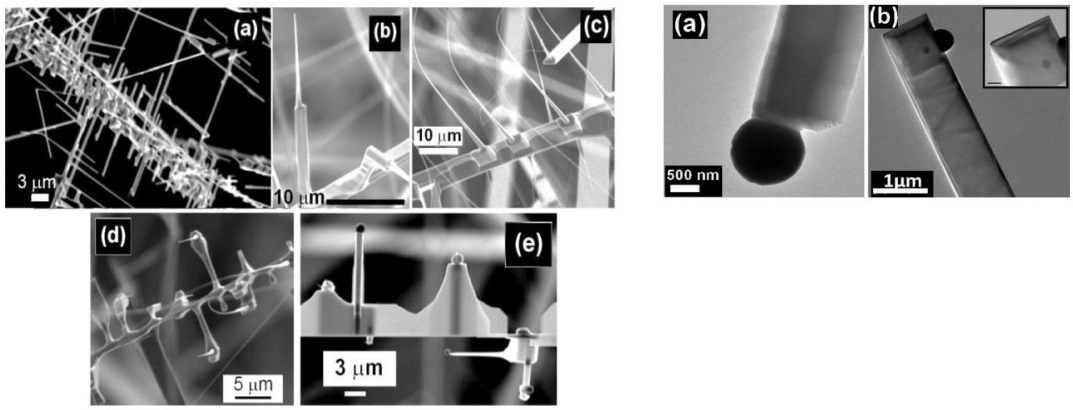

Figure 3.3 - Left side: SEM (Scanning Electron Microscope) images of the nanostructures grown when doped in presence of SnO_2. Right side: SEM image of a branch of the doped nanowire [18]

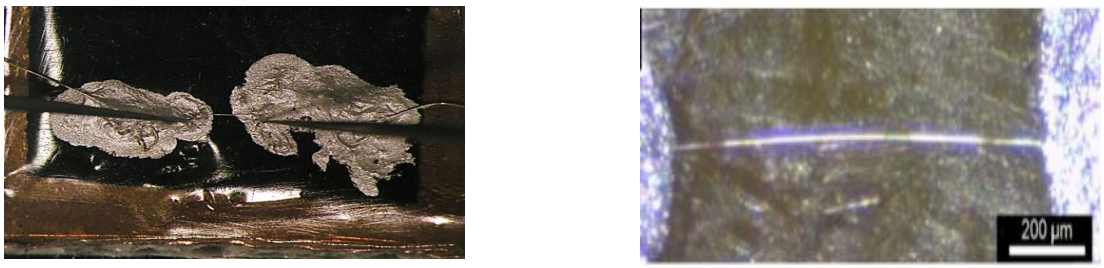

Figure 3.4 - Left side: Nanowire tested in this work, with silver contacts and microprobes of the parametric analyzer. Right side: an amplified image of the nanostructure.

The doped gallium oxide nanowire are grown by a two-step thermal oxidation process:

1) The nanowires are grown by the vapor-liquid-solid (VLS) method, where pellets were made of compressed Ga_2O_3 powders of 99.999% purity and were used as a substrate for the metallic gallium precursor. This process was done in a tubular oven, for 10 h, at 1150 ^oC with a flux of Argon of 0.8 l/minute.
2) The second step, were the doping was achieved, the samples produced were put in the oven first at 1100 ^oC, for 1 hour, and then again for 1500 ^oC, for 15h, both with a flux of Argon of 0.8 l/minute and in the presence of metallic gallium and SnO_2 powder.

The Gallium oxide nanowire doped with tin show higher electrical conductivity since Sn is an efficient n-type dopant in Ga_2O_3 [18].

The nanowire studied in the present work has a silver contact has shown in Fig. 3.4 (left side) and has 800 micrometer length (same figure, right side) and 900 nanometer radius [18].

3.2 **Molybdenum trioxide**

Molybdenum trioxide crystals have a wide band gap between 2.9 and 3.2 eV. Both flakes and nanoplates, were grown in the α-MoO_3 phase (see Fig. 3.5), confirmed by high resolution transmission electron microscopy (HRTEM)[19].

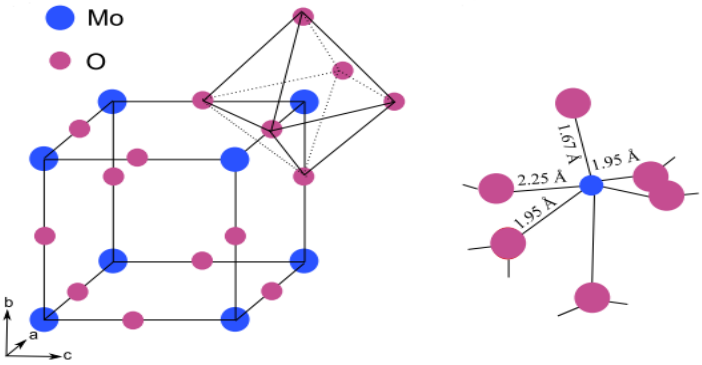

Figure 3.5- Crystal structure of molybdenum trioxide [20].

Molybdenum trioxide crystal flakes (see Fig. 3.6) were grown by the VS (Vapor-solid) process, compacting under a compressive load a powder of pure molybdenum and without any precursor, for 10h at 750 ºC, with a flux of air of 1.2 l/m, in a tubular furnace ,by the group of Material's physic, at the *Computalense University* from *Madrid* [21]. The flakes present a laminar structure with a structural anisotropy where Mo-O bonds have distances between 1.67 to 2.33 Å which are directly related to the ability for the oxidation state of Mo. [21]

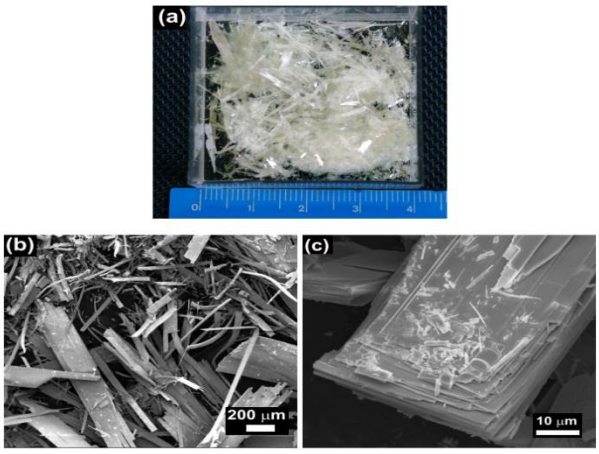

Figure 3.6 - (a) Photograph of laminar crystals (b) and (c) SEM images of the flakes evidencing the laminar structure of the grown crystals [21].

In SEM images (Fig. 3.6 c) the laminar structure of the flakes can be observed. This characteristic allowed exfoliated samples to be produced by mechanical exfoliation (using the scotch tape technique).

The Molybdenum oxide nanoplates were grown by the same method as the flakes, the VS method, but the thermal treatment was done at 800 ^{o}C, for 40 minutes with an Air flux of 1.2 l/min.

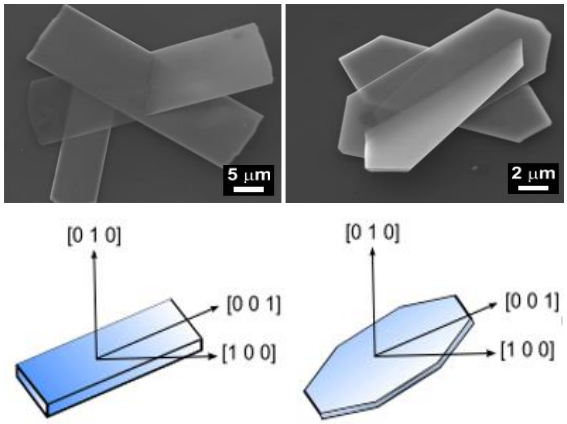

Figure 3.7 - SEM images of MoO3 nanoplates with rectangular shapes and hexagonal shapes and respective crystal axes [21].

The air flux favors the transportation of the material to a low temperature region inside the walls of the tubular furnace, where the material sets and starts to nucleate forming the nanoplates.[21]

The samples' thickness studied in this work (Table 1), were determined by Rutherford Backscattering Spectrometry (RBS), where measuring the areal density of the layer and using the density of MoO_3 from literature [21], allowed the calculation of the typical width of the nanoplates and of the MoO_3 flakes produced by mechanical exfoliation (using the scotch tape technique), assuming the density of the flakes, nanowires and bulk is the same.

Table 1 – Thickness of the MoO_3 samples studied

Density of MoO_3	$4.69\ \frac{g}{cm^3}$	
Areal Density determined by RBS	Nanoplate	$200\ \frac{\mu g}{cm^2}$
	Exfoliated Flake	$2900\ \frac{\mu g}{cm^2}$
Thickness	Nanoplate	400 nm
	Exfoliated Flake	6.48 μm

4

Techniques and experimental setup

In this chapter, the main techniques used to characterize and to modify the samples are summarized.

A new home-made chamber in the Van de Graff accelerator, conceived by LATR (CTN) team, is used for electrical in-situ measurements simultaneously with several other techniques, namely RBS, PIXE and ion luminescence. Annealing processes were performed in an ANNEALSYS AS-One Rapid Thermal Processing cold wall chamber furnace. The proton beam experiments were developed at the Plasma and Nuclear Fusion Institute (IPFN), situated at the Laboratory of Accelerators and Radiation Technologies (LATR) inside the Nuclear and Technological Campus (CTN) of Instituto Superior Técnico (IST).

4.1 **Electrical characterization. Parametric Analyzer.**

The current versus voltage (*I-V*) curves were measured using an Agilent B1500A parametric analyzer, used in general for semiconductor device characterization. The parametric analyzer measures the *I-V* curves, and I (t) curves, current as a function of time, for a constant applied voltage. It is equipped with 4 MPSMU (Medium power source/monitor unit) which allow voltages up to 100V to be used simultaneously. In order to do the correct measurements and with as little noise as possible, the correct connectors had to be installed. SMU can be connected to electric contacts, such as crocodile clips or the micro positioners, by tri-axial cables because an extra layer of insulation is a requirement when very low currents (such as nA and lower) are going to be measured.

The 20 micrometers movement resolution micro positioners from Everbeing provide fine adjustments in all 3 dimensions and were associated with one micrometer tungsten tips (T20-10). This metal tip can provide the electric contact directly on top of

some samples. These tips are very useful in order to perform instant and safe contacts of very little structures preventing damage and without making permanent contacts. In order to make measurements as reproducible as possible and for example avoid effects of charge accumulation during the measurements, a rectangular voltage function is applied to the sample with the time of zero voltage much longer than the time of voltage applied; 20 ms voltage on and 180 ms voltage off.

4.2 Microbeam and the new Setup

The Van der Graff generator can produce a beam of 2.5 MeV protons or alpha particles. The Van de Graff accelerator is equipped with three beam lines that allow the use of techniques such as RBS, PIXE and IL. The nuclear microprobe (*Oxford Microbeams®)* allows focusing the beam by means of quadrupole magnets *reaching* lateral resolution of 1.5 μm. The lateral resolution enables the analysis of small and heterogeneous samples with more precision and as is the case of the structures used in this thesis. To these techniques was added the electrical characterization for measurements *in-situ* using the parametric analyzer (Fig. 4.1).

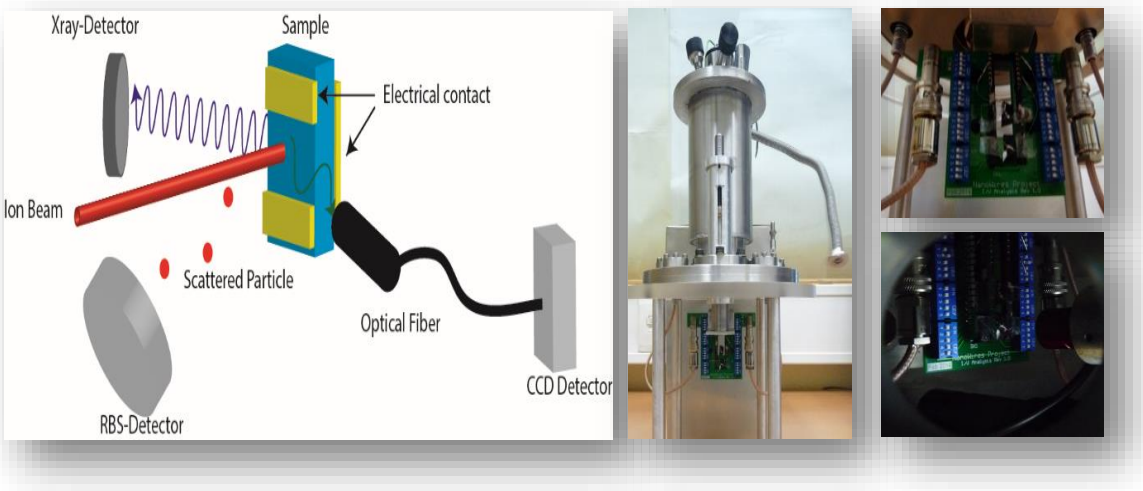

Figure 4.1 - Left: Scheme of the combined techniques and overview of the new setup. Middle: the new chamber lid; Right: amplified views of the printed circuit board (PCB) for the electrical measurements.

The figure 4.1 provides an insight of the new setup. The new chamber lid (middle) allows the alignment of the samples in height and incidence angle.

4.3 Rutherford Backscattering Spectrometry (RBS)

Rutherford backscattering spectrometry (RBS) is a nuclear technique that is widely used for surface analysis of solids. Basically a target is bombarded with ions (typically alpha particles or protons of 0.5 to 4 MeV energy). The energy of the backscattered ions, coming from the surface and from the bulk, are measured in a solid state detector giving information on the elemental composition of the layers with a depth resolution of several nm at the surface. The energy of the backscattered particle, coming from the surface, is given by a simple relation between the energy before and after the collision, where the k factor, or kinematical factor, gives the ratio between the two.

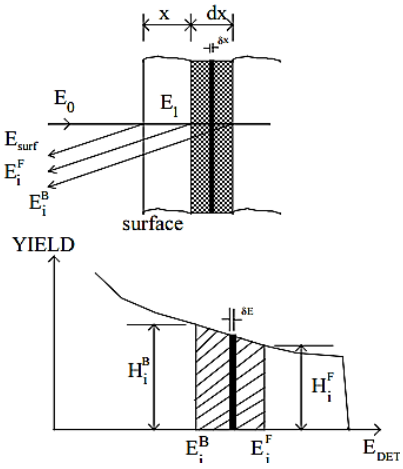

Figure 4.2 - RBS schematic of the physical principle behind backscattered particle and the relation between the energy and depth of the material.[22]

The difference between the energy of the backscattered particles coming from the bulk, at a certain depth, and from the surface can be related in order to determine the sample thickness (see schematic in Fig. 4.2). The parameters involved and dependent on the material properties are the kinetic factor and the stopping power [23].

4.4 Particle Induced X-Ray Emission (PIXE)

PIXE is a nuclear technique that determines the elemental composition of a material, by analyzing the X-Ray emission prevenient from the atomic interactions when the sample is exposed to an ion beam. Since X-rays are specific for each element the composition of the samples can be determined. While RBS gives more depth information about a material, PIXE is useful to distinguish elements with similar mass and it is very sensitive to low concentrations of contaminants.

In a resumed way, when a charged particle (from the beam) enters the material it will perform several elastic and inelastic collisions losing its energy along the trajectory, quantified by the stopping power of the material. The ionized atoms will produce X rays

with a probability given by the cross section and if they suffer little attenuation, they will emerge from the surface (see schematic in Fig. 4.3).

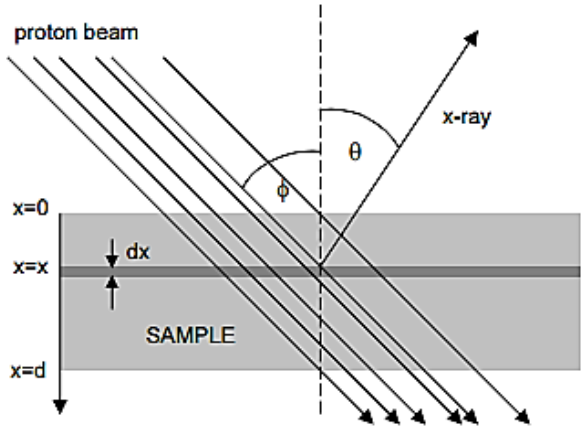

Figure 4.3 - PIXE schematic of the physical principle behind X-ray emission from the sample[22].

Both PIXE and RBS were used mainly to position the samples while being irradiated and to give an estimation of the samples thickness.

4.5 Annealing Process

Rapid thermal annealing (RTA) processes can achieve temperatures over 1000 ^{o}C, in few minutes or less, using high power lamps or lasers. In the present work, an ANNEALSYS As-one furnace was used. This furnace can perform annealing from room temperature to 1500 ^{o}C, with ramp rates up to 200^{o}C/s in different atmospheres (Ar, N, air) and in high vacuum (up to 10^{-6} mbar) [24]. Annealing processes are known for many applications especially for semiconductor technologies once they can change interfaces, change steps of growth, repair damage caused by ion implantation [2] and relocate/activate dopants in films. So RTA can improve the quality of contacts by improving the adhesion of the metal and reducing the presence of defects [25].

4.6 UV Lamp

Using a High Power UV-Vis Fiber Light Source, L10290 model of Hamamatsu, with a deuterium and a tungsten/halogen lamp providing light with wavelengths between 200 nm and 1600 nm, respectively UV radiation and infrared.

Table 2 - High Power UV-Vis Fiber Light Source lamps - L120290 [26]

Lamp	Wavelength [nm]	Energy [eV]
Deuterium	200 – 400	6.2 - 3.1
Tungsten/Halogen	400 -1600	3.1 – 0.78

Attached to the light source, there is an optical fiber to serve as a conductive medium for all wavelengths. This light source possesses a shutter that allows to choose if one wants to use visible light prevenient from the tungsten/halogen lamp, the UV light from the deuterium lamp or both at the same time. This mechanism also allows changing the lamps between each other without turning them off, since these lamps need time to heat up and stabilize.

5

Electrical Characterization

Gallium oxide and molybdenum oxide are intrinsic n-type semiconductors [27] [28]. A description of semiconductors will be given in the next section and the generality of crystalline semiconductors physics will be briefly described. Conductive mechanisms and junctions will be reviewed in order to understand the current-voltage characteristics of the devices.

In metals, and according to the band theory of solids, the valence and conduction bands overlap. The Fermi level is at the top of the occupied states in the conduction band. In semiconductors, on another hand, the valence and conduction bands are well separated by a bandgap (E_g) (Fig. 5.1). At zero kelvin, electrons are all in the valence band, but at room temperature some electrons have enough energy to overcome this gap and fill available quantum states in the conduction band.

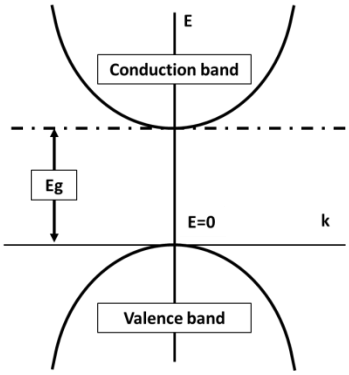

Figure 5.1 - Scheme of a typical band structure for a semiconductor.

Insulators have the same characteristics as semiconductors, but their band gap energy is too high to be overcome by thermal excitation. However, there are no fixed rules on how to distinguish semiconductors from insulators. Many materials nowadays considered wide band gap semiconductors, were once called insulators.

When electrons are excited to the conduction band (CB), holes are being created in the valance band (VB), leading to currents of negative charges (electrons) and currents of positive charges (holes) in opposite directions, *i.e.*, they are bipolarized. In pure semiconductors there is an equilibrium between electrons in the CB and holes in the VB. This equilibrium can be changed by doping the semiconductor with impurities giving rise to different conduction behaviors, dependent on the type of impurities: electron donors or electron acceptors, creating energy states within the bandgap closer to the conduction band (n-type semiconductor) or closer to the valence band (p-type semiconductor).

5.1 **Semiconductor-Metal junctions**

Metal-Semiconductor contacts were first comprehensively described by Schottky and for that reason Metal-Semiconductor devices are called Schottky barrier devices. This description is usually applied to devices where the current-voltage characteristics are clearly non-ohmic. One way to describe the semiconductor-metal junction at their interface is by aligning their Fermi energy level [1].

Two different contact behaviors can occur between a metal and a semiconductor; and as said before, it can form a Schottky contact with a rectifying behavior or it can form an ohmic contact.

When an n-type semiconductor is brought in contact with a metal, the Fermi levels align and electrons flow from the semiconductor to the metal causing a band bending at the semiconductor-metal interface (Fig.5.2). The potential barrier build up in this way will eventually stop this electron flow and equilibrium is reached. Here, assumptions are being made that surface states are not playing a major role in the contacts established.

Electron diffusion takes place because of the different chemical potential of the last filled levels of both materials. Electrons can flow from the semiconductor to the metal without any given energy until they accumulate in the regions closer to the interface and an opposite electric field appears canceling the spontaneous flow, so an energy given by ϕ_{SB} (called the Schottky barrier) has to be given so the barrier can be overcome (see Fig. 5.2).

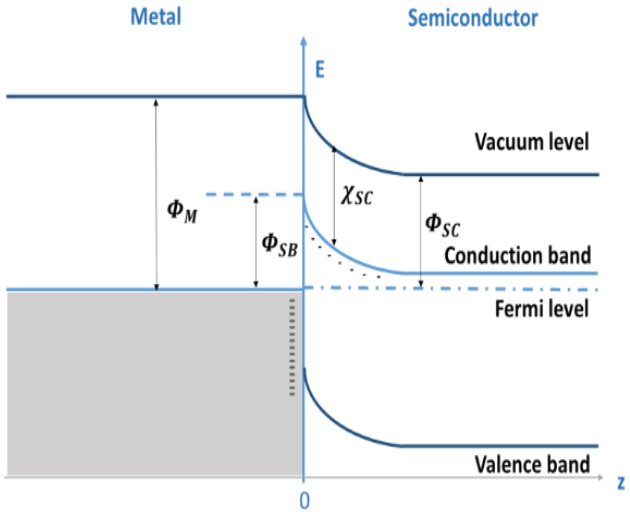

Figure 5.2 - One dimensional energy diagram for the interface region of a metal semiconductor junction after contact

In Fig.5.2 Φ_M, represents the work function of the metal,Φ_{SC}, is the work function of the semiconductor,χ_{SC}, represents the electron affinity of the semiconductor and Φ_{SB}, represents the energy of the Schottky barrier considering that only bulk effects are participating on the represented n-type semiconductor-metal junction. The Schottky barrier is highly dependent on the quality and purity of the interface area (a region of a few nanometers between the semiconductor and the metal), as well as the number of surface state.

When equilibrium is achieved, the energy of the Schottky barrier, ϕ_{SB}, is given by comparing the energy difference between the work function of the metal, ϕ_M, and the electron affinity of the semiconductor,χ_{SC}

$$\phi_{SB} = \phi_M - \chi_{SC} \qquad (5.1)$$

Ohmic contacts are established between a highly doped semiconductor and a metal, where the charge concentration reduces the band bending given by ϕ_{SB}.

5.2 Schottky diodes current-voltage characteristic

When two metal contacts are put at the ends of the semiconductor (see Fig. 5.3), and a voltage is applied, a series of Schottky diodes is created, being one device directly polarized and the other reversely polarized.

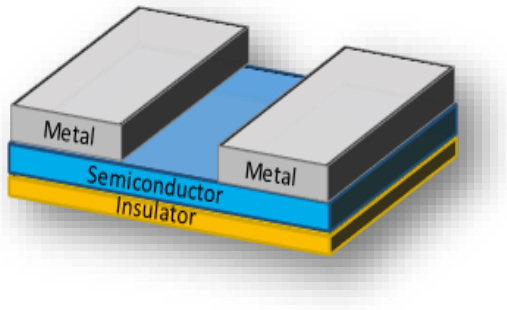

Figure 5.3 - Top view scheme of a metal semiconductor metal (MSM) configuration used to make the devices in this study. It has a layer made of an insulator material that was the substrate for the crystal (semiconductor) and two metal contacts deposited on top.

This configuration is called back-to-back Schottky devices [3]. The devices are usually referred to as metal semiconductor metal (MSM) devices.

5.3 **Contacts produced and results**

For the in situ electrical characterization measurements of Ga_2O_3 and MoO_3 while being either irradiated with charged particles or excited with UV light, MSM devices were made. For the present case it did not matter if the contacts were rectifying or ohmic, because the main goal was to make stable contacts. As for the case of gallium oxide it was relatively easy to establish contacts, but many attempts were made in order to measure the conductivity of the molybdenum oxide flakes until some conclusive measurements could be done. Although gallium oxide has a wider band gap and one would think it would be more difficult to do the MSM junction, molybdenum oxide flakes are far more brittle than the gallium oxide crystals and therefore far more difficult to make a M-S junction. In the next paragraphs the procedures made in order to establish the contacts and the *I-V* characteristic curves of each device will be described. The first contacts were made in bulk samples due to the facility of making contacts in bigger samples and to understand the material behavior before the production of thinner samples.

Due to the brittleness of both crystals, hard insulator substrates, like glass, proved to be inadequate for measurements with the micro positioners because the tips would disrupt in pieces. Since these devices were going to be irradiated with high energy protons, scotch tape was not a good solution as well.

The substrate chosen was Kapton Tapes, made from Kapton ® polyimide film with silicone adhesive, suitable for temperatures up to 300 ^{o}C, proton irradiation and with capability of sustaining the samples. Schematics of the device structures are shown in Fig. 5.4.

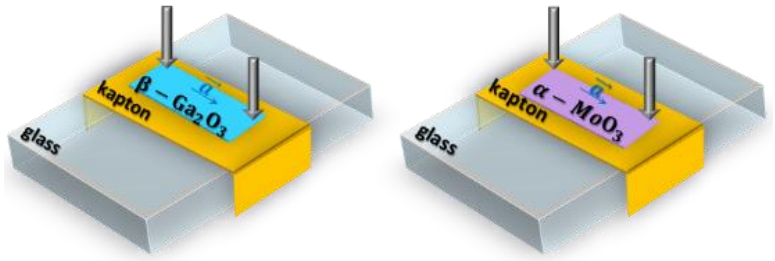

Figure 5.4 - Scheme of the device built for testing gallium oxide and molybdenum trioxide crystals with kapton as a substrate and with tips

Many tests were carried out in order to check the absence of ion conductivity for this tape, since nonzero ion conductivity was reported in reference [29]. Fortunately, the irradiation did not lead to current flow in the tape, probably due to the fact that the silicone adhesive side was not conductive and not sensitive to proton irradiation.

From the available materials, those with closer work function to the band gap of gallium oxide (~4.9 eV)[5] and molybdenum oxide(~3.2 eV) [30] were chosen. The similarity between these potentials decreases the resistance of the Schottky contact and consequently decreases the necessary potential difference across the device necessary to get current flow. [31]

Aluminum, silver, tungsten, gold, indium and tin contacts were tested.

The indium used to make contacts is from GoodFellow and has a high purity. The aluminum used is traditional aluminum foil and the tin used is traditional soldering material.

To the semiconductors glued with the Kapton tape, bits of each of the metals available were deposited on top, with the help of tweezers, has can be observed in Fig.5.3, allowing the electrical studies ahead to be performed.

Contacts and samples were then annealed in a tubular furnace, at 200 ºC, for six minutes, in air, for the tin, aluminum and indium metals in both crystals.

None of the metals made a good MS junction, which is probably due to an oxide insulator layer created during the annealing exposed to the oxygen in the atmosphere.

In order to address this, the same contacts were tested for both semiconductors using a rapid thermal annealing furnace in controlled ambient.

The MSM devices were annealed at 200 ºC, for 120 seconds in a vacuum of 1×10^{-5}mbar.

For both cases only the indium metal produced a good contact, probably due to its high purity and low melting temperature. However, the contacts present a lot of noise. In order to address the noise of the measurements more annealing treatments were done

in the same conditions to the same samples but for higher temperatures and longer times.

The *I-V* characteristic curves for the RTA results for the indium contacts can be observed in Fig. 5.5. For both semiconductors it's represented the first annealing, at 180 ºC for 120 sec, and for the last annealing, performed at 200 ºC, 240 sec, both at 1x10^{-5} mbar. As can be observed in the right plot of Fig.5.5, there is a lot of noise for both semiconductors.

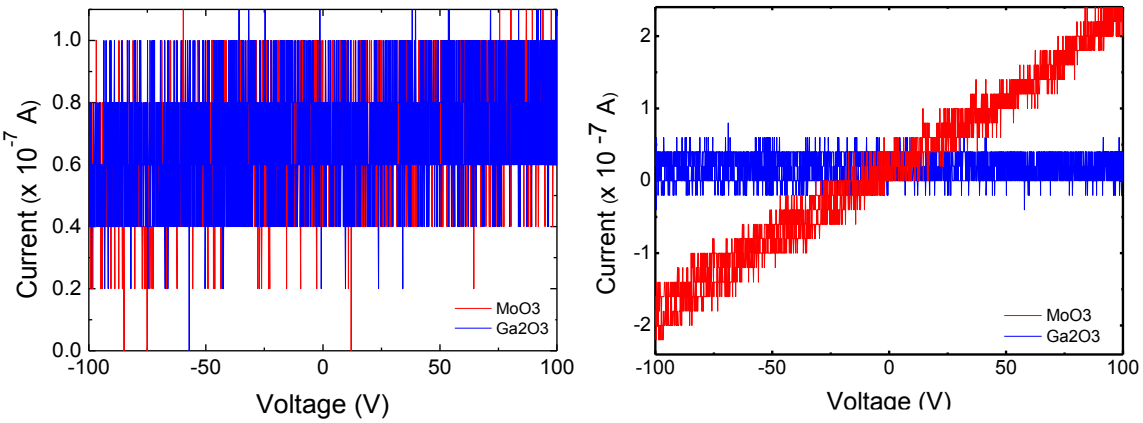

Figure 5.5 - Ga_2O_3 and MoO_3 with indium contacts annealed in Rapid Thermal Annealing (RTA), at 1x10^{-5} mbar Left: 180 ºC, 120 sec and Right: 200 ºC, 240 sec

Comparing the right and left plots, the gallium oxide sample did not reveal any improvement using this approximation.

However, for the case of the molybdenum oxide sample, a clear change can be observed.

In order to understand if this was a material response more annealing tests were performed in another sample made in the same conditions.

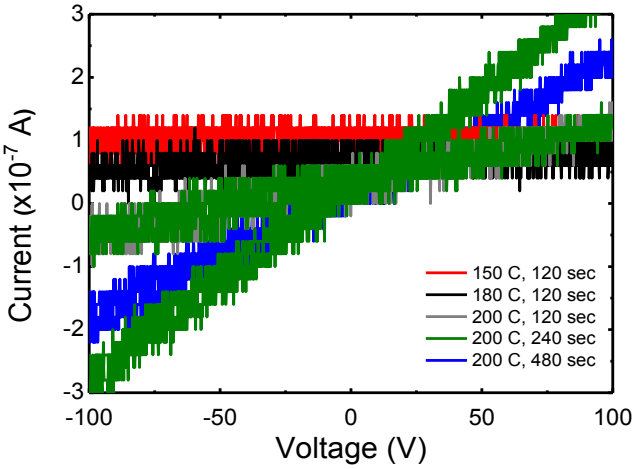

Figure 5.6 - Annealing tests performed in RTA for a second sample of molybdenum trioxide, for increasing temperatures and exposition time.

The same results were observed for this second sample and are shown in Fig. 5.6. In this plot is also evidenced the electrical hysteresis typical of bath quality contacts. For example, the green curve belongs to one current-voltage measurement and shows two different branches were one belongs to positive current and another to negative current. If the contact was well made, the resistance of the sample would be the same since the measuring conditions are the same.

For both samples the conductivity is seen to increase with annealing temperature and, in contrast to Ga_2O_3, an ohmic behavior is observed.

Another phenomenon that can be observed in these samples concerns the lifetime of the sample conductivity after annealing. It was noticed that these samples lose their conductivity a day after the annealing and even with the contact being established. In Fig. 5.7 *I(V)-t* curve, can be observed that for the same applied voltage, of -90 V, the sample current suffered a decrease of 86% 12 hours after being annealed . The samples recover to an insulating state although it would still have a slightly higher conductivity than the unannealed sample.

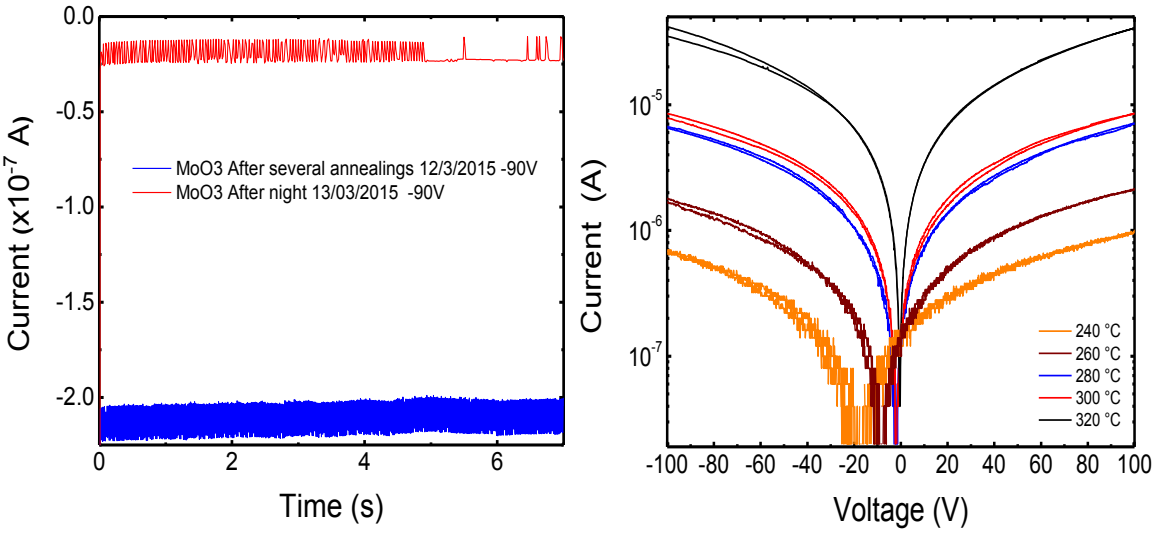

Figure 5.7 - *I(V)-t* curve Left: sample with contacts loose conductivity one day after being annealed. Right: test of the influence of temperature of annealing on the conductivity of the contacted sample

A logarithmic scale was applied to the *I-V* plots of annealing tests performed for increasing temperatures (Fig. 5.7 right). The current is increasing with increasing annealing temperature and the contact become better as evidenced in the lower noise and more symmetric curves.

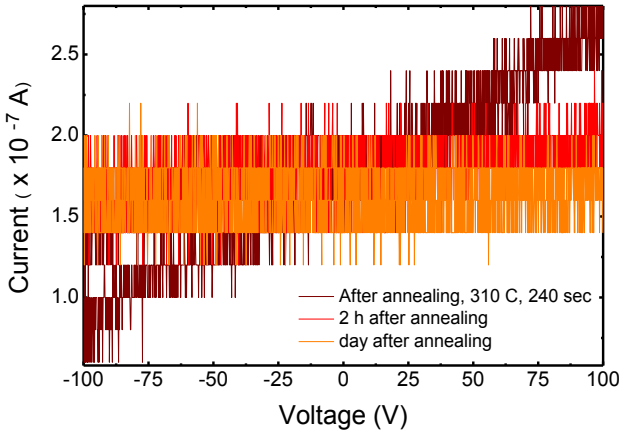

Figure 5.8 – *I-V* test of the influence of temperature of annealing in the conductivity of the non-contacted sample

In order to understand if this was due to the presence of indium, where it could have evaporated during the RTA process and then deposited over the sample, the same tests were performed in non-contacted samples using tungsten tips (See Fig. 5.8). The same behavior was measured showing that annealing must alter the material itself and

not only the contact. The recovery behavior took place again, decreasing about 75% from the maximum current measured for 100V.

The creation of oxygen vacancies during annealing may explain such behavior since they are known to be donors in most metal oxides. On the other hand, the slow recovery of the initial state may point to adsorption effects at the surface, meaning oxygen molecules or other adsorbents are returning to the surface of molybdenum oxide. [6].

The reason behind this different reaction between gallium oxide and molybdenum trioxide crystals, might be attributed to the crystal's production temperature where gallium oxide crystals were produced at approximately 1500 ^{o}C and molybdenum trioxide flakes were produced at approximately 800 ^{o}C.

For the case of Gallium oxide crystal flakes, the best work setup found was with the silver ink from circuit works®.

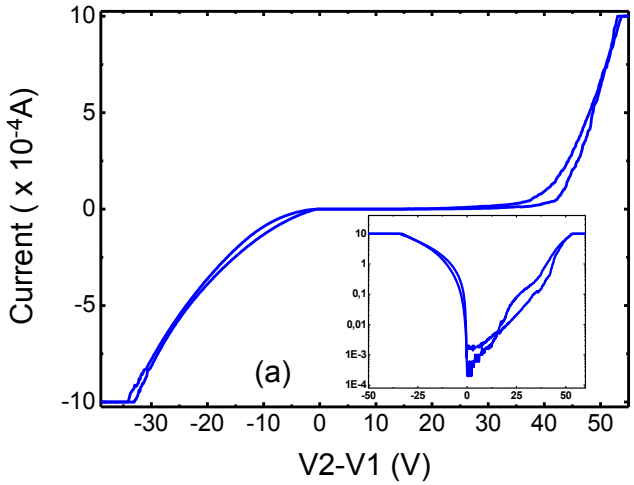

Figure 5.9 - *I-V* curve for a gallium oxide sample with silver contacts

The silver ink is liquid and solidifies at room temperature. This ink was directly deposited on top of the gallium oxide crystals and the typical *I-V* curves obtained can be seen in Fig. 5.9. No annealing's were performed in this devices since the ink is polymeric and evaporates.

A current limitation was set in order to preserve the contacts and the material. The limit settled was 1 mA and corresponds to the saturation lines that take place when the voltage is around -30 V or 50 V.

A logarithmic scale has been proved useful to compare device polarizability answer to direct bias and to reverse bias, as can be seen in the inset in Fig. 5.9. If the contacts were equal the curve would be symmetric and as can be observed, the contacts are not equal.

In the following paragraphs a possible explanation about this phenomenon will be given.

Being contact nº1 at zero Volt, when the applied tension in contact nº2 is negative, the conventional current flows from contact nº1 to contact nº2, and it encounters a resistance different than when it flows from contact number 2 to number 1. This means that one contact is offering more resistance to the passage of current than the other and this resistance depends on the direction of the current flow (as expected for a Schottky diode).

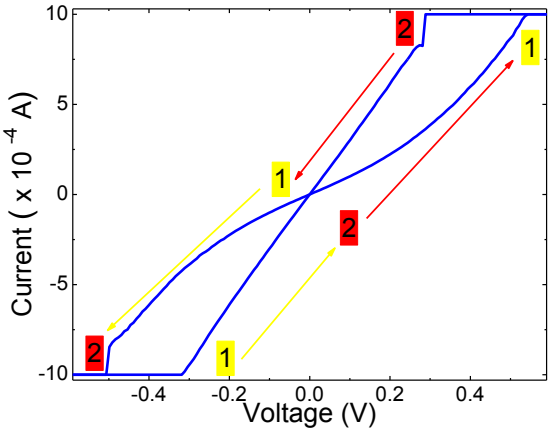

Figure 5.10 - *I-V* curve situations where the current flows from contact nº1 to contact nº2 and vice-versa.

In Fig. 5.10 it is represented in yellow the experimental values for which the current flows from contact nº1 to nº2, and in red it's represented the opposite path. This means that for each yellow path, the 1st contact is directly polarized and the 2nd contact is reversely polarized. For the red lines the opposite is true.

So it can be observed that the contact number one is offering more resistance when reversely polarized.

When the contact is directly polarized the current flows without much effort from the metal to the semiconductor when the potential difference is high enough to overcome the Schottky barrier (thermionic effect). However, if in this circuit the current flows from the semiconductor to the metal , this contact is reversely polarized and the energy necessary to overcome it is not only the one given by thermionic effect but is also due to field effect emission [3].

We can conclude so far that to make contact with Ga_2O_3, silver ink is a good solution because it is relatively cheap (at least half the price of a silver sheet/wire and a third of the price of a gold leaf/thread) and it is also easy to handle.

The contacts were stable, adhering, which led to reproducible *I-V* curves with low-noise levels.

The same device configuration was developed for exfoliated samples and for nanowires and proved to be a good setup for future irradiation studies, although some thermal evaporation of metal contacts had been done they prove to fail in terms of the crystals endurance for successive studies, since thin layers with hundreds of nanometers did not present the robustness needed for the study of these materials.

To further understand the conduction mechanism of the samples, some tests were performed taking into account the three possible spatial orientations as shown in Fig. 5.11 for gallium oxide samples with silver contact.

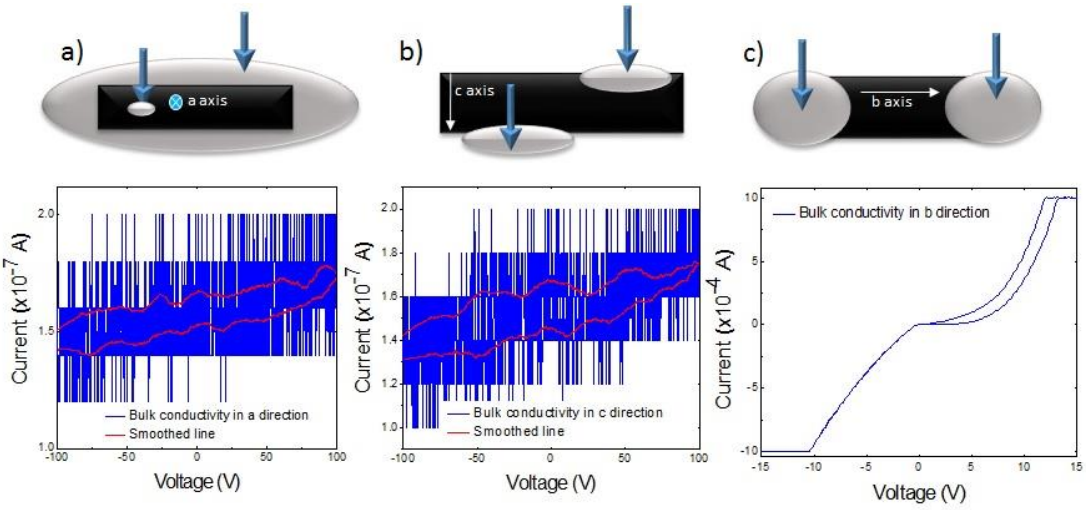

Figure 5.11 - Schematic of the three contact configurations performed with silver (represented in grey) and Ga_2O_3 (represented in black) and respective *I-V* curves for a) bulk conductivity along the a crystal axis b) conductivity in the c direction crystal axis and c) conductivity in the direction b crystal axis.

For *I-V* a) and b) curves correspondent to the geometry defined below each plot, were smoothed (red solid line) in order to understand better the *I-V* curves despite the high noise level.

For the cases represented in a) and b), in Fig. 5.11, the currents measured are of the order of 10^{-7} A, and for the case represented in c), the current measured achieves values three orders higher than for the first two contact configurations. Also, a) and b), show a lot of noise and hysteresis, were in c) this phenomena is smaller. The contacts were produced in the same manner, so the conductivity along the axis given by a) and b) are negligible relatively to the axis given by c).

Concluding, these measurements set a good base to evaluate that the main contribution for current flow is along the b crystal direction (<010>) of the gallium oxide samples studied. This might be in line with the STM image of the electronic domains showed

in Chapter 3, were three different electronic distributions can be observed in the different crystal orientations.

For the case of molybdenum oxide samples, a similar procedure with indium contacts was made and in the c axis it showed increased conductivity while for the conductivity along the bulk and the a axis direction it showed no conductivity, however, these measurements were not conclusive because the samples were highly damaged during the measurement due to their high level of brittleness.

The devices that ultimately showed better working conditions (less noise, few hysteresis, stable and reproducible measurements) and used to perform the irradiation studies are given in Table 5.1.

Table 5.1 – Devices produced and used for irradiation tests

Sample Characteristics					**Tests Realized**			
Devices Studied	**Dimensional Limit**	**Dimension**	**Contacts**	**Substrate**	**I(t)**	**UV(air)**	**Proton (2nA) (Vacuum)**	**Vacuum Test**
					Voltage Applied (V)			
Ga_2O_3	**Flakes (2D) - non irradiated sample**	[0.83 x 0.21 cm]	silver ink	kapton tape	-10	-10		
	Flakes (2D) - irradiated sample	[0.74 x 0.18 cm]	silver ink	kapton tape	-10	After proton irradiation: -10	-10	
	Nanowires(1D)	[900 nm x 800 um]; thickness =900nm	silver ink			-10	60	
MoO_3	**Flakes (2D)**	[92.3 µm x 246 µm]; thickness = 10 µm	indium	kapton tape	-10		-10	
	Nanoplates (2D)	[340 µm x 800 µm]; thickness = 5 µm	indium with traces of lead and copper	sapphire	2	2	2	2

6

Radiation -Matter Interaction

Radiation is the emission of energy as electromagnetic radiation, such as heat radiation and X-rays, or the emission of energy as moving subatomic particles, in particular high-energy particles, which can cause ionization of the medium. In this work, we are particularly interested in phenomena using ultra-violet (UV) radiation and energetic ion beams.

6.1 Electromagnetic radiation-matter interaction

Several phenomena can occur during electromagnetic radiation-matter interaction; namely, absorption, photoelectric effect, Compton Effect, pair production among others, dependent on the photons energy and on the atomic number and electronic density of the material [32]

In absorption, the medium will absorb some of the energy carried by the electromagnetic wave attenuating the intensity of incident beam as it passes through the material. The intensity of the incident radiation decreases exponentially with distance travelled in the material and it is described by the Lambert-Beer law:

$$\frac{I(l)}{I_0} = e^{-\frac{4\pi k}{\lambda} lc} \qquad (6.1)$$

Where k is the extinction coefficient, λ is the wavelength of the radiation used, l is the path length made by radiation beam and c the concentration of the absorbent substance in the medium. To the energy carried by the electromagnetic field, there is associated a photon of energy:

$$E_{ph} = h\frac{c}{\lambda} \qquad (6.2)$$

In a semiconductor, an electron in the valence band absorbing the energy of the photon can acquire enough energy to jump to the conduction band, if the photon energy is equal to or higher than the bandgap. When the conduction band has a minimum at another position than zero for the k vector of the Brillouin Zone, i.e. in an indirect-gap semiconductor, a higher energy than E_G is required for this transition or an additional phonon needs to be absorbed by the electron.

When an electron is excited to the conduction band, a hole is also created in the valence band. After excitation with electron can either recombine directly with a hole in the valence band or it can form an exciton. In this case, the electron is attracted to the hole and a bound state is created where both particles revolve around their center of mass. This attraction diminishes the energy difference between the electron and hole levels falling slightly below E_G.

Also free carriers can absorb radiation without being excited to another band due to available quantum states more favorable in the same band. These are called intraband transitions. When semiconductors have impurities, those can influence the degree and type of absorption. There can be shallow impurities whose energy levels are closer to the conduction band and deep impurities that capture the charge carriers and change the conductivity of the material.

6.2 **Ion-Solid Interaction**

In case of an energetic ion-beam, the particles traveling through the material will transfer some of their energy to the material (nuclei or electrons) by elastic or inelastic collisions that can result in crystal structure breakups or electronic excitation of the material's atoms, giving rise to changes in the electronic properties. In this work, we focus on the electronic changes since our main purpose is to study the conductivity properties and behavior. Due to the charge of the particles, the interaction ion-material is of Coulombic nature (electric nature).

Particles will go through the material, depositing energy along their path and if this medium is sufficiently thick, these particles will be totally decelerated and their energy totally absorbed by the medium.

The collisions can be of different natures depending on the beam energy and on the distance to the nucleus at which the collision happens. This distance is named the impact parameter (b).

6.3 **The Stopping Power**

The energy transferred by one particle per unit path length in the medium is called the stopping power-dT/dx. Firstly described by Bohr, the stopping power was written in terms of the kinematic factor, which takes contribution of the mass and electronic charge per unit volume of the medium and the velocity of the incident particle [22]. But a quantum mechanical and statistical approach was needed and Hans Bethe provided it considering the mean excitation potential of the atom and another function for the contribution of velocity for the stopping power [22]. This formula also allows relativistic concepts to be included by corrections to the velocity term. However, the mean excitation potential is not given by a single theory, because there would have to be knowledge of every ground and excited state. In these terms, Felix Bloch showed that the mean excitation potential can be approximated by statistical methods [22]

Those theories combined, will describe the decreasing energy of an ion when passing a medium, according to the Bethe-Bloch formula. Adding the Bragg's Rule for compounds, total stopping power can be described by the linear combination of the stopping powers of individual elements.

Because of the large amount of unknown variables for calculations of each materials stopping power values, simulations using Monte Carlo algorithm have been extensively used to preview the right stopping power characteristics for a large amount of materials and the values simulated are not far from those calculated with an estimated 2% error.

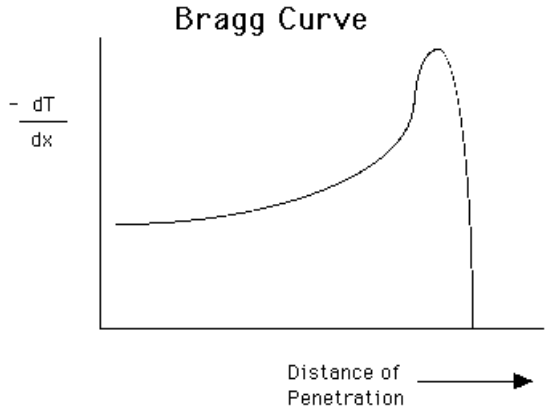

Figure 6.1 - Typical Bragg Curve represented as a function of the distance accomplished for a light energetic particle in a heavy matrix.

A typical electronic stopping power curve is represented in Figure 6.1, as a function of the distance accomplished for a light energetic particle in a heavy matrix. The maximum in the plot corresponds to the Bragg peak. The depth at which the energy

transfer is maximum, and the maximum penetration depth of the protons can be estimated from the stopping power curves.

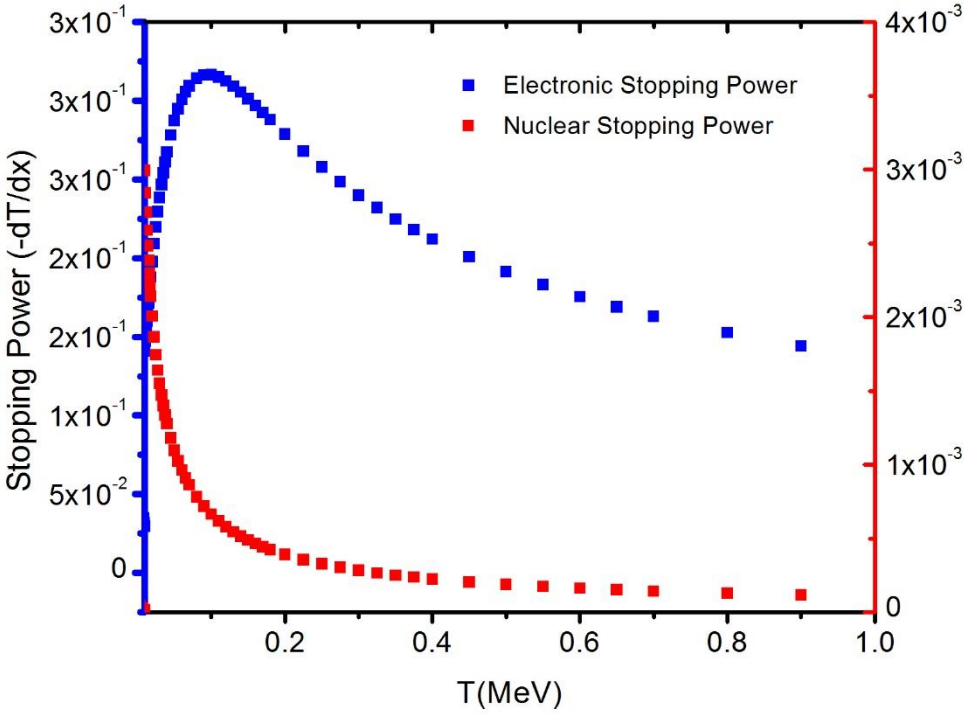

Figure 6.2 - Comparison between nuclear (red data and red scale) and electronic stopping power (blue data and blue scale) for protons in gallium oxide.

In Fig. 6.2 nuclear and electronic stopping power curves, for gallium oxide irradiated by a proton beam, as a function of the energy of the beam are represented. The curves were obtained using the Stopping and Range of Ions in Matter (SRIM) software. As one can observe the electronic contribution is much more relevant than the nuclear contribution for the case of 2 MeV beam. The peak means that the energy for which the particle loses more energy to the material is at 0.1 MeV.

6.4 Simulation of Proton Irradiation Profiles

Since the materials investigated in this thesis are being studied in terms of being sensors of irradiation, ion impact profiles were studied.

The simulations of ion beam bombardment were performed using the Monte-Carlo code for the Transport of Ions in Matter (TRIM) [33]. This software simulates binary collisions between incoming ion and target atoms that will give the distributions of implanted ions and implantation induced defects. The simulations provided by TRIM are well accepted in the scientific community, having provide accurate results, as can be understood from Fig.6.3 for the irradiation profile of gallium and molybdenum (both solid)

with hydrogen ion beam, where the plots correspond to the experimental and simulation (black solid line) data for many values of beam energy [33].

For 2 MeV proton beam in gallium and molybdenum it is shown that a maximum of 10% uncertainty is expected for the hydrogen ion beam.

However this comparison is just relative to the heaviest elements in the crystal structure that are studied in this work, because the crystals were not found in the literature and since stopping power depends proportionally on the atomic number (Bethe-Block equation) it seems an acceptable correlation to be made).

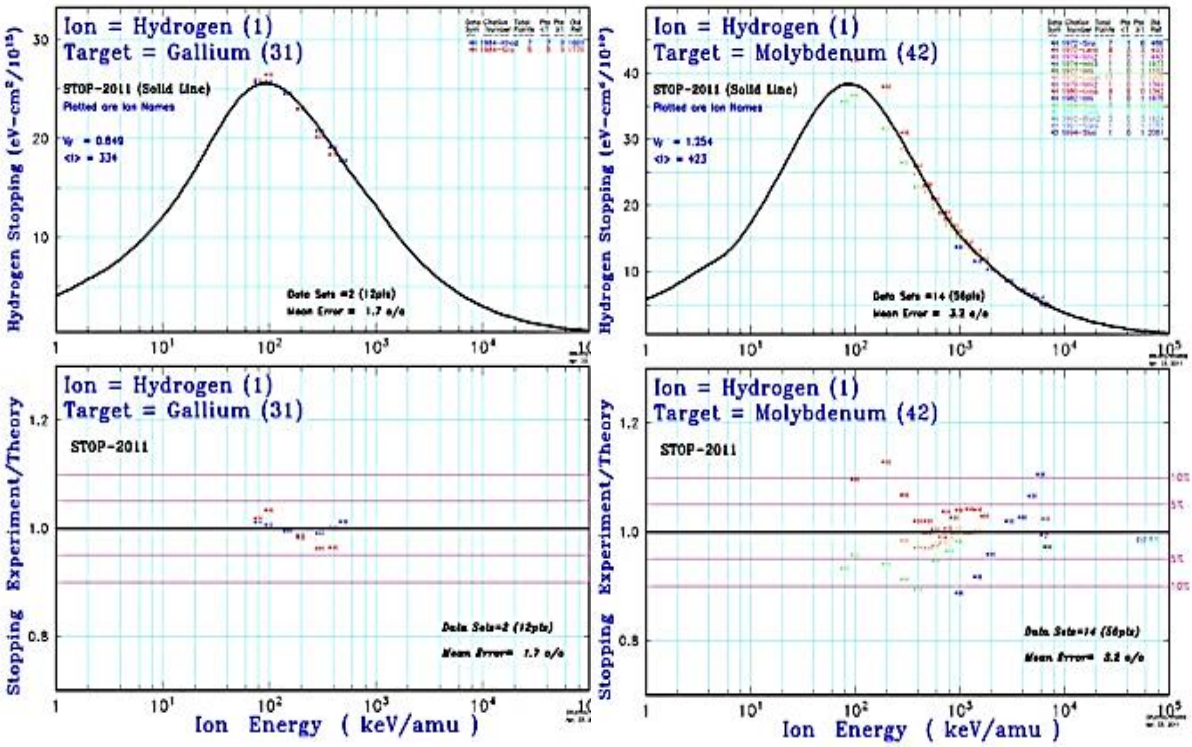

Figure 6.3 - SRIM simulation plots for stopping power for hydrogen ion irradiation for a gallium target (top left plot) [47] and for molybdenum target (top right plot) [48].

However, TRIM does not take into account inhomogeneous surfaces, nor does it take into account laterally asymmetric samples [34]. For instance, in Fig. 6.4 the errors that are being made if simulations for nanostructures are being made assuming a bulk structure instead of the real geometry of a nanostructure can be observed.

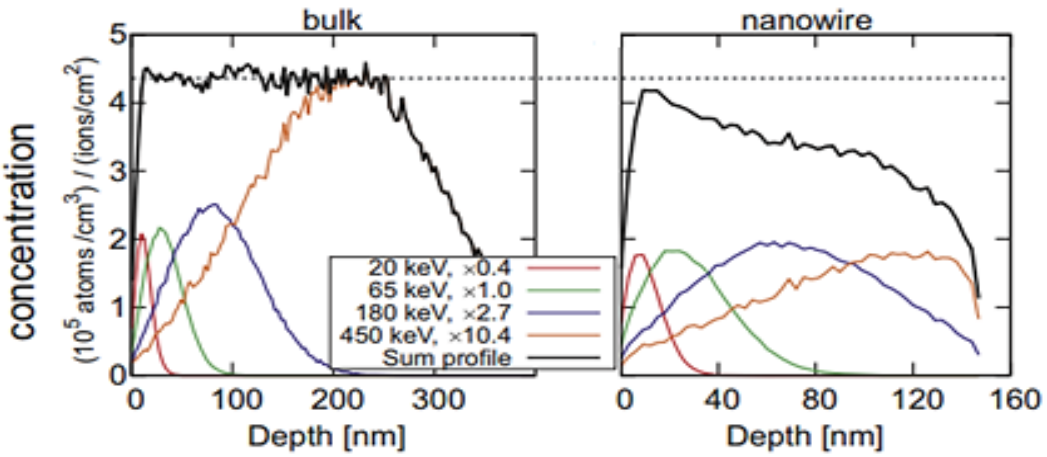

Figure 6.4 - Comparing SRIM simulation assuming a bulk geometry (left) and using the program Ion Range And Damage In Nanostructures (Iradina) [34] assuming the correct geometry of a nanowire.

If the simulations are being made in the SRIM ambient, they will not take into account the geometry of the sample, like for case of nanowires with diameters of hundreds of nanometers as used in this study.

So for nanostructures, irradiation profiles had to be simulated using Iradina (see Fig. 6.4) and bulk structures by Transport of Ions in Matter (TRIM).

For the case of bulk gallium oxide and molybdenum oxide structures, the irradiation with a 2000 keV ion beam of H^+ ions (protons) were simulated.

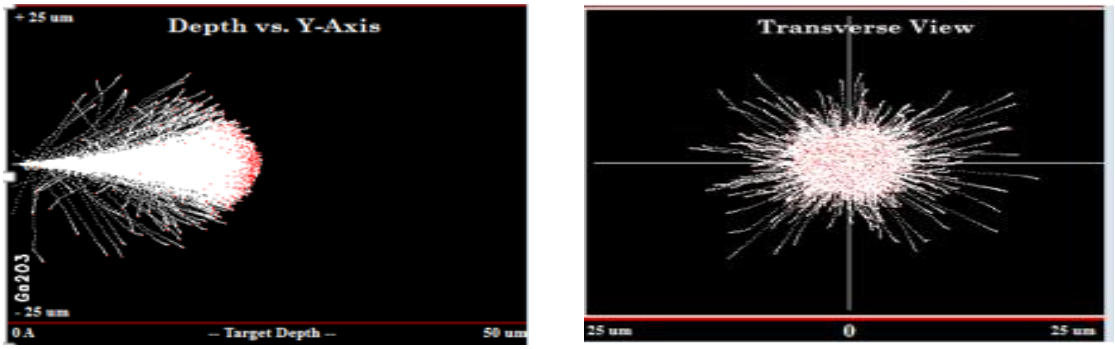

Figure 6.5 - TRIM simulation showing the ion tracks with depth and in transverse view for a 2 MeV proton beam in Ga_2O_3

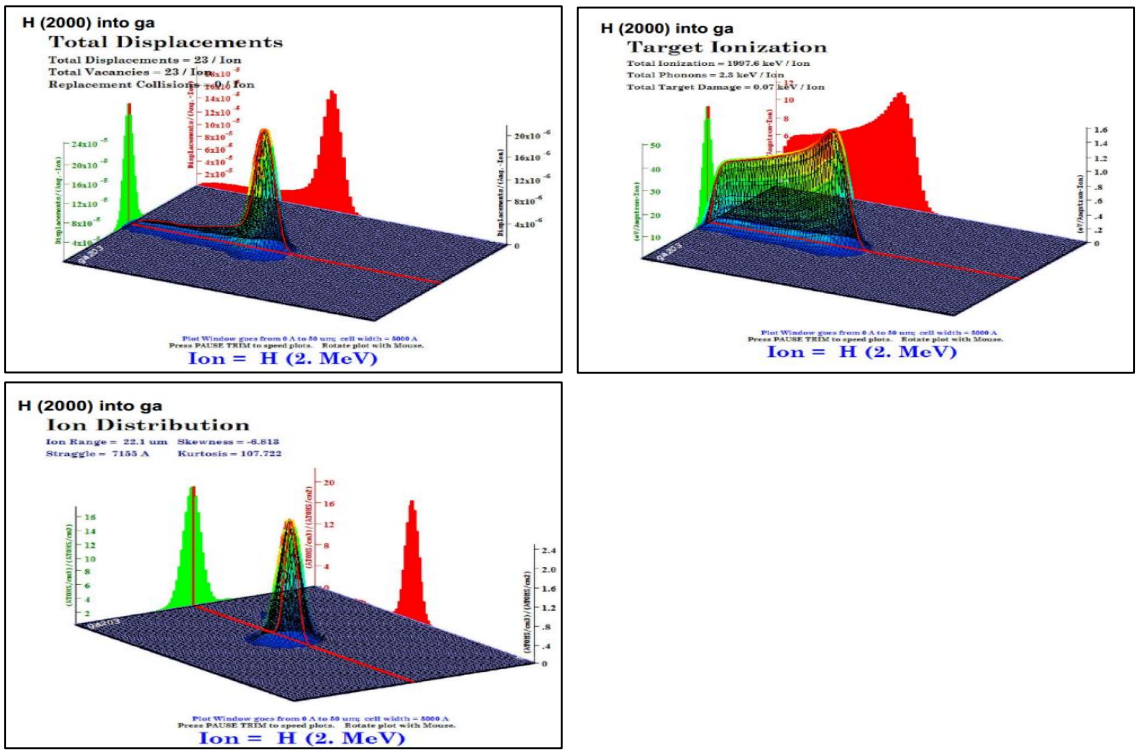

Figure 6.6 -Total displacements of both gallium and oxygen caused by the passage of the beam; Ionization profile in gallium oxide by the electronic collisions with the ion beam, distribution of protons in gallium oxide.

For the Ion Distribution in the gallium oxide layer, for a 2 MeV proton beam, it will be with a higher probability totally stopped by the target atoms at the depth of the Bragg peak. Simulations yield a projected range of 22 μm and a straggling of 7890 Angstroms.

In terms of ion beam induced conductivity, the most relevant plot is the Target Ionization, which gives a good visualization of the amount of atoms that are being ionized in the material by the electronic component of the stopping power.

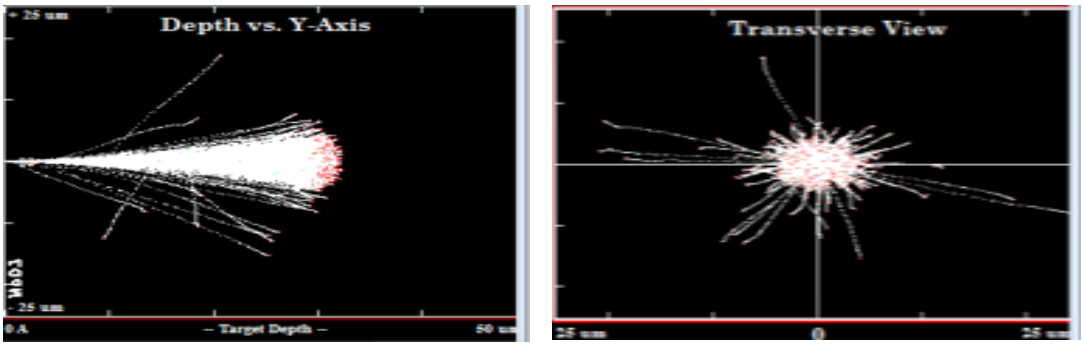

Figure 6.7 - TRIM simulation showing the ion tracks with depth and in transverse view for a 2 MeV proton beam in MoO

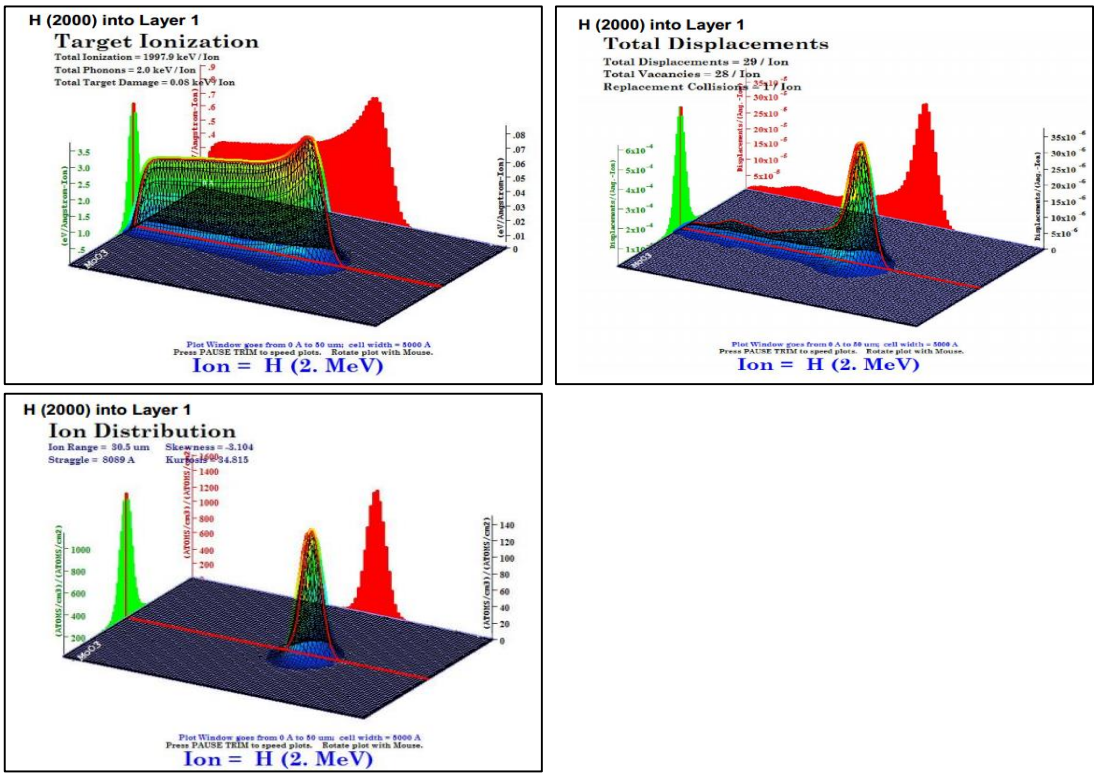

Figure 6.8 - Ionization profile of molybdenum oxide caused by the passage of the 2MeV proton beam in molybdenum oxide; Total Displacements of both molybdenum and oxygen, Proton distribution in molybdenum oxide.

For the Ion Distribution in the molybdenum trioxide layer, for 2 MeV protons, simulations yield a projected range of 30.5 μm with a straggling of 8089 Angstrom near the Bragg Peak.

In the same figure, the Total Displacements plot simulates the number of molybdenum and oxygen atoms that are being removed from their positions, again the nuclear

component of the stopping power is making the displacements of target atoms through elastic collisions between the target nuclei and the ions.

On average, for each proton being bombarded into the sample, 29 atoms are being displaced.

Simulations for an irradiation of a nanowire of Ga_2O_3 (radius of 900 nm and irradiated from the side facet) by a 2 MeV proton beam were performed using the Iradiana code. Results are shown in Fig. 6.9 where the images represent the amount of energy deposited in the nanowire by inelastic electronic energy loss and by the energy loss by recoils.

It is seen that the electronic energy deposition is homogeneous throughout the nanowire thickness and that very few displacements occur (see Fig.6.10). It makes sense that not many effects are observed in terms of displacements since the nanowire has a radius of 900 nm and the range for 2 MeV protons in gallium oxide is 23 micrometers.

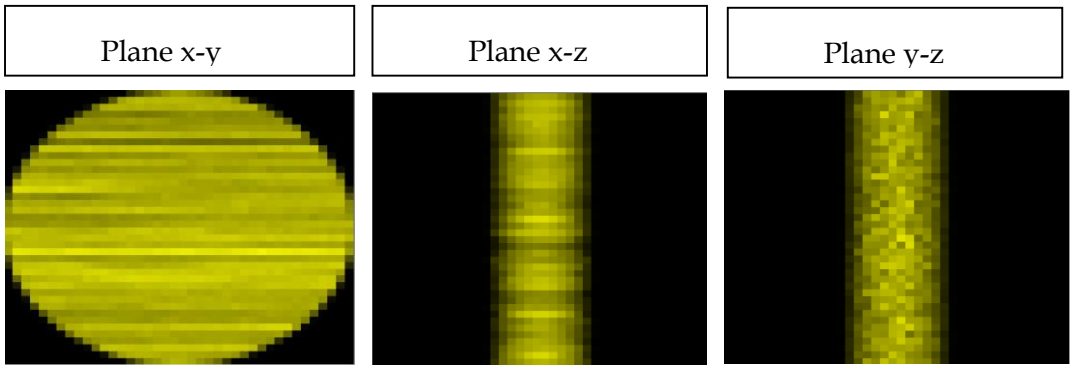

Figure 6.9 - Ionization profile of the nanowire where the beam enters the nanowire perpendicular to the x-axis.

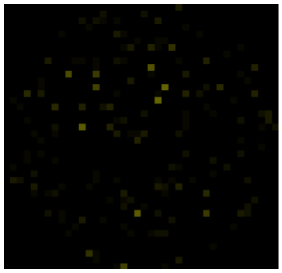

Figure 6.10 - Displacements of gallium and oxygen along the x-y plane of a 900 nm diameter Ga_2O_3 nanowires irradiated with 2 MeV protons.

7

Ion luminescence

Flakes of gallium oxide were irradiated with protons of 2 MeV kinetic energy with the incident beam perpendicular to the crystal (see Fig. 7.1).

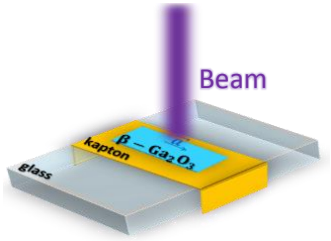

Figure 7.1 - Relative position of the incident ion beam to the crystal.

Under proton irradiation, it was observed that the gallium oxide emits blue light.

It was also reported that in addition to the intense blue band $\beta - Ga_2O_3$ emits in the UV and green spectral region [35].

The blue emission has been attributed to oxygen vacancies and complexes involving oxygen vacancies, which are the main native defects [13].

$\beta - Ga_2O_3$ also presents other intrinsic defects where donor states can also be provided by interstitials of gallium (with energy levels between 0.03 – 0.05 eV below the conduction band) and Gallium-Oxygen vacancy pairs originate acceptor levels within the band gap [35].

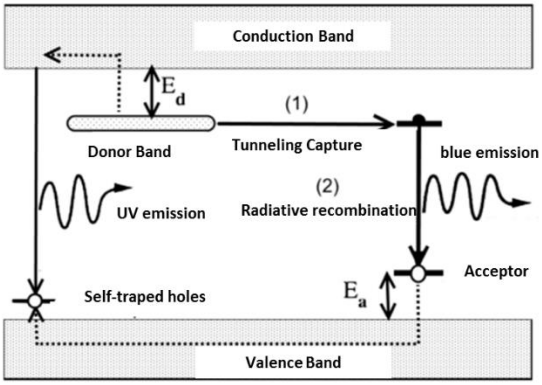

Figure 7.2 – $\beta - Ga_2O_3$ luminescence mechanisms schematic (from [35]).

One of the models proposed for the blue luminescence (see Fig. 7.2), by Binet and Gourier [35], relates the luminescence with the tunneling capture of electrons provided by the oxygen vacancy donor states to the neutral acceptor state and subsequent recombination with the holes of the acceptor states provided by V_{Ga}-V_O pairs [35].

PIXE and RBS spectra were acquired during proton irradiation (Fig. 7.3)

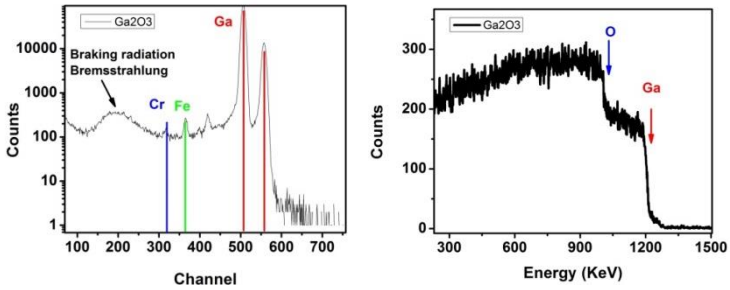

Figure 7.3 - PIXE and RBS spectra for a gallium oxide sample irradiated with 2 MeV protons

From the RBS spectrum, it was estimated that the sample was thicker than 20 microns, because otherwise, the barrier would have an ending and not be the continuous retrodispersed particles' energy spectrum that can be observed.

By the PIXE spectrum, it was assured that the sample was in fact being irradiated and emitting the characteristic Kα and Lα lines correspondent to each of the present elements. The Kα (9.25174 keV) and Lα (1.09792 keV) lines of gallium were identified and oxygen cannot be identified (being this one of the limitations of PIXE) due to its transition energies being totally absorbed by the medium. Chromium and Iron belong to the contacts.

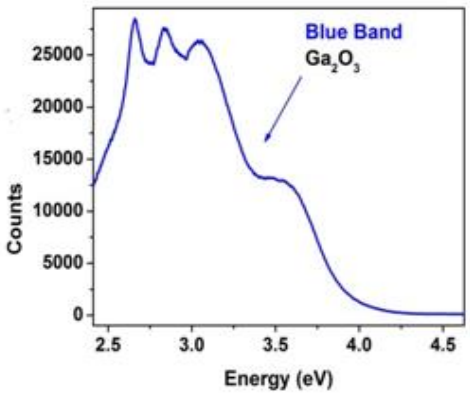

Figure 7.4 - Ion Luminescence spectrum from the Ga_2O_3 material when being irradiated (horizontal scanning) with protons.

In figure 7.4, the luminescence spectrum, under proton irradiation, is shown. The UV and blue emission of the gallium oxide flake under proton irradiation can be observed, where it is shown from 2.5 to 4 eV approximately.

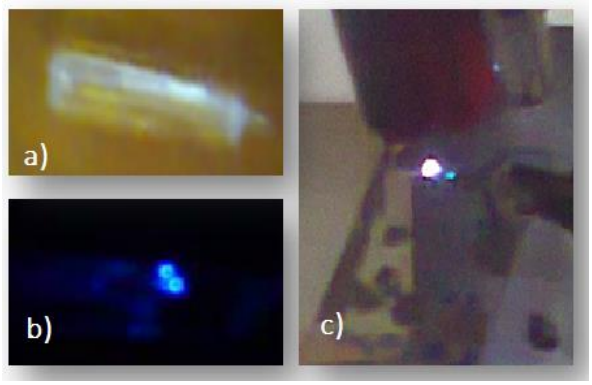

Figure 7.5 – a) Picture of the gallium oxide flake b) blue emission during proton irradiation (lateral beam scanning) c) blue emission observed during irradiation with UV light.

Fig. 7.5 shows pictures of the blue emission observed during UV excitation in air (c) and proton irradiation in vacuum (b), showing that similar processes occur when using these different irradiation conditions.

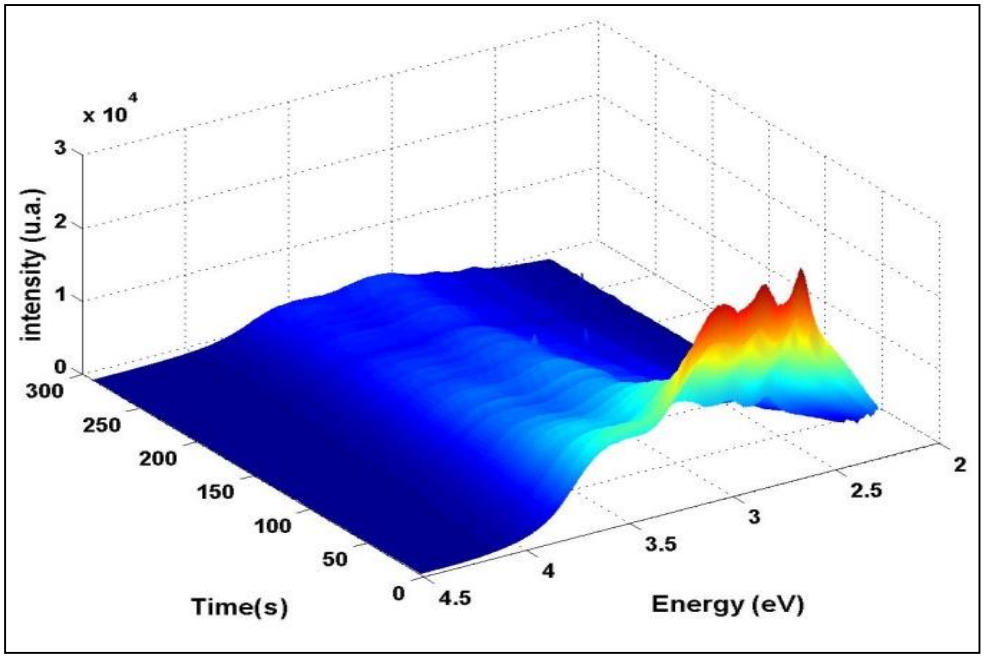

Figure 7.6 – Final 250 seconds of the luminescence spectrum of the gallium oxide during proton irradiation.

It was observed that the intensity of the blue luminescence decreases along the irradiation probably due to the formation of deep level defects that act as non-radiative recombination centers (see Fig. 7.6).

Since the beam is highly energetic, the contribution for the first 20 micrometers depth inside gallium oxide will be mainly electronic (causing target ionization) and nuclear collisions take place mainly around a 1 micrometer wide region around the Bragg peak at that same depth, causing major displacements of the gallium and oxygen atoms (as determined by the SRIM simulations in Chapter 6). At this stage it is not clear if and how electronic interaction is contributing to the quenching of the blue luminescence. It may change the charge state of native defects and alter their luminescence properties, however, such processes are usually of reversible nature.

8

Radiation Induced Conductivity (RIC)

Radiation Induced Conductivity (RIC) can take place when a semiconductor is exposed to radiation and can be monitored by measuring the current when a constant voltage is applied to the material.

The changes on RIC depend on many factors such as temperature, applied electric and magnetic fields, and on the energy transfer phenomena [36]. Moreover, it depends on the electronic structure of the material –semiconductor/isolating materials. In semiconductors, electrons in the valence band can be excited to the conduction band increasing the number of free carriers available, leaving a hole in the valence band. Other phenomena, such as localized trap states, can contribute for the control of charge mobility and conductivity, as happening in highly disordered insulating materials (HDIM), with localized trap states, distributed in space and energy [29].

In cases of a beam of energetic charged particles, the collisions can be of electronic or nuclear nature. For the first few microns of the proton path inside the material, interactions will be between the proton and the electron cloud of the target atoms, giving rise to a variation in the charge distribution of the material. However, nuclear interactions can also take place, as reported in Chapter 6, and defects caused by elastic collisions can alter the atomic distribution of the material, causing permanent defects that will give rise to energy levels inside the forbidden band, changing permanently the conductive behavior of the semiconductor.

In the case of excitation with photons -light beam- it might be given enough energy to overcome the band gap or excite electrons from defects closer to the conduction band, and causing the conductivity also to increase.

However, for both UV and proton irradiation, excited electrons have lifetimes associated and eventually will decay to more stable energy states. Therefore, the number of electrons and holes will change with time. As free carriers are being continuously created in time, they will also recombine with each other and annihilate continuously as well. This recombination times will give rise to a current that is persistent.

8.1 **Persistent Photoconductivity (PPC)**

Persistent Photoconductivity that is caused by the excitation of a semiconductor by a light source, leads to a current that can persists in time and can last until several days, depending on the material [37]. It can be due to several phenomena namely impurities, defects [38] or confinement of conduction electrons by molecules at the surface causing band bending [39].

For the case of an n-type semiconductor, the high energy levels created by the donors, often called high energy level traps, can donate electrons to the conduction band just by room temperature, allowing the continuity of the current even after the source that it's promoting the conductivity to be removed.

For the case of oxide semiconductors, the oxygen vacancies are said to be responsible for the n-type nature of the semiconductor and the electrons that belong to this vacancies are behind the increase of the conductivity when the semiconductor is excited with light [40].

As reported for zinc oxide based sensors for UV light [40], oxygen molecules will adsorb on the surface of the semiconductor, capturing electrons from the conduction band as oxygen ions, 0^{-2}, and acting as an electron trap. The accumulation of negative charge particles at the surface give rise to a depletion layer that causes band bending and confines the electrons on the center of the conduction band at the surface.

When the device is irradiated, photo generated holes migrate to the surface recombining with electrons at the O_2-related trap states and allowing excess electrons to move freely in the material's core and narrowing the depletion layer.

$$h\nu \rightarrow e^- + h^+ \qquad (8.1)$$

Neutralized O_2 easily desorbs from the surface and an equilibrium of adsorption and desorption is responsible for the saturation of the photocurrent.

$$O_2^-(adsorbed) + h^+ \rightarrow O_2(g) \qquad (8.2)$$

Slow re-adsorption processes after the light is switched off can then explain the persistent current [41] [40].

The variation of electron concentration in the conduction band in time after switching off the excitation source is given by [42]:

$$\frac{dN(t)}{dt} = -k(t)N(t) \qquad (8.3)$$

Where $k(t)$ is the time dependent transition rate parameter of conduction electrons to a lower energy level and N(t) is the number of electrons which were excited to the conduction band during the irradiation. Integration of this expression gives:

$$N(T) = N_0 e^{-\int_0^t k(t)dt} \qquad (8.4)$$

The current intensity is assumed to be proportional to N and the normalized current is given by:

$$I(t) = \frac{N(t)}{N_0} \qquad (8.5)$$

So I(t) can be described by:

$$I(t) = e^{-\int_0^t k(t)dt} \qquad (8.6)$$

The model used for the treatment of the decay time is the Kohlrausch stretched exponential analysis represented by equation 8.7 and frequently used for physical decay processes involving time dependent decay rate coefficients k(t) [43].

$$k(t) = \frac{\gamma}{\tau}(\frac{t}{\tau})^{\gamma-1} \qquad (8.7)$$

Where γ lies between zero and one and τ is the time constant. The meaning of γ depends on physical models underlying the studied processes but generally a smaller value of γ corresponds to a wider distribution of transition rate parameter k(t), suggesting a more disordered system [44].

Substituting 8.7 in 8.6 gives:

$$I(t) = e^{-\left(\frac{t}{\tau}\right)^{\gamma}} \qquad (8.8)$$

As reported in other works, the same type of treatment can be achieved for the case of the rise of the current [45].

For each case the equations used to do the analysis of the *I(V)-t* characteristic curves will be:

Rise:

$$I(t) = I_0\left[1 - e^{-\left(\frac{t}{\tau_{ON}}\right)^{\gamma}}\right] \qquad (8.9)$$

Decay:

$$I(t) = I_0 e^{-\left(\frac{t}{\tau_{OFF}}\right)^{\gamma}} \qquad (8.10)$$

8.2 **Persistent Ion-Conductivity (PIC)**

In the present work, proton irradiation studies were performed using a 2 MeV proton beam.

As seen in chapter 6, this beam will dominantly interact by means of inelastic collisions between the beam and the electron cloud of the sample's atoms, ionizing the atoms of the medium. As the beam loses its energy, it will interact with the medium by elastic collisions that take place between one ion from the beam and one atom from the lattice, causing the atom to move from its position and to initiate a collision cascade. The inelastic collisions are more probable around 20-22 micrometers for gallium oxide and around 30 micrometers for the molybdenum trioxide, which corresponds to their Bragg peaks, but ,as observed in the simulations showed in Section 6.4, there is also a probability of occurrence along the path of the beam inside the material.

When the beam passes through the material, energy transferred by elastic collisions will cause the electrons to be excited from the valence band to the conduction band and the behavior is similar to that explained in the photoconductivity chapter where an increase in conductivity with a persistent behavior, can be observed.

However, at the same time inelastic collisions are taking place, creating defects by that can cause the material to be permanently damaged along the path of the beam, even if at low probabilities.

So, many effects are taking place in this process: increase in conductivity, damage of lattice structure and persistent conductivity [7] but it's assumed the phenomena explained in Section 8.1 for conductivity (adsorption of oxygen molecules at the surface) is the same for both photo and ion-conductivity.

In order to compare the different effects caused when exciting the sample with UV light or when irradiated with a 2 MeV proton beam, the Kohlrausch stretched exponen-

tial analysis model ,given by equation 8.7, and that is commonly used for PPC (UV), will be used for PIC (proton).

8.3 **Persistent Induced Conductivity – Experimental Results**

The results obtained for gallium oxide and molybdenum trioxide, flakes, nanowire and nanoplates, will be presented in the next section for the excitation measurements with UV light and for the irradiation with the 2 MeV proton beam.

The beam current used was 2 nA, corresponding to 1.25×10^{10} protons being irradiated onto the samples per second.

The beam was set up perpendicularly to all the samples studied and it covered all the surface of the semiconductors that constituted the devices.

The results acquired during irradiation will be presented in *I(V)-t* curves, where a constant voltage is applied to the device and the current is measured in time, and in *I-V* curves, where the current is measured setting different voltages and measuring the respective currents.

In the presented figures, the *I(V)-t* curves are shown as insets and correspond to the actual measurements taken while the samples were being excited or left to relax. The periods while the sample is being illuminated with the ultraviolet light or irradiated with the proton beam correspond to On periods, and the resting times, while the illumination source is turned off and the beam is removed from the sample, correspond to Off periods. One cycle of On/Off periods, is represented with yellow and grey respectively in each inset plot.

For further data analysis the data was normalized and excitation times and relaxation times were treated separately as described in detail below. In the presented figures, the grey data lines and grey y (left y axis) and x (bottom x axis) scales, correspond to the normalized decay curves and the black lines and black y (right y axis) and x (top x axis) correspond to the normalized rise times of the various cycles represented inset.

For clarity, only one fit of one cycle is represented, and the results from the fitting of the rise and decay curves, using the equations 8.9 and 8.10 for the PPC model, will be analyzed in detail in the next section (8.4).

The metal contacts on top of each sample were individually irradiated with UV light and the conductivity of any of the devices in study did not show any difference, so the contacts are not contributing to the PPC phenomenon of the tested samples, as expected.

8.3.1 Ga_2O_3 2D UV

Flakes (2D) of gallium oxide devices (non-irradiated flake Ga_2O_3, Table 5.1, Chapter 5) with silver contacts, were obtained from bulk gallium oxide (Chapter 3), and were exposed to UV radiation in air. The current intensity of the device, was measured, *in-situ*, using the parametric analyzer, for a constant applied voltage of -10V. The current intensity versus applied voltage (*I-V* curves) was measured and compared before and after irradiation and during UV excitation, where the sample was totally irradiated with the UV light, using the optical fiber close to the sample. The background light was checked to not contribute to the conductivity of the device, nevertheless the measurements were done under the shielding provided by an aluminum box. Using the tungsten lamp the sample was exposed to visible and infrared light from 400 nm (3.1 eV) up to 1600 nm (0.78 eV), corresponding to energies below the bandgap of Ga_2O_3 (4.8 eV), and no photo conductivity was observed for this device in such conditions.

In the inset of Fig 8.2 a steep increase of the current can be observed when the light is switched on due to the photo-generated free charge carriers.

When the sample recovers from the period of excitation (OFF), persistent photoconductivity phenomena can be observed. The initial current value for the device is $I_t = 1.5 \times 10^{-4}$ A and when it is irradiated with UV light it increases up to $I_t = 1.9 \times 10^{-4}$ A.

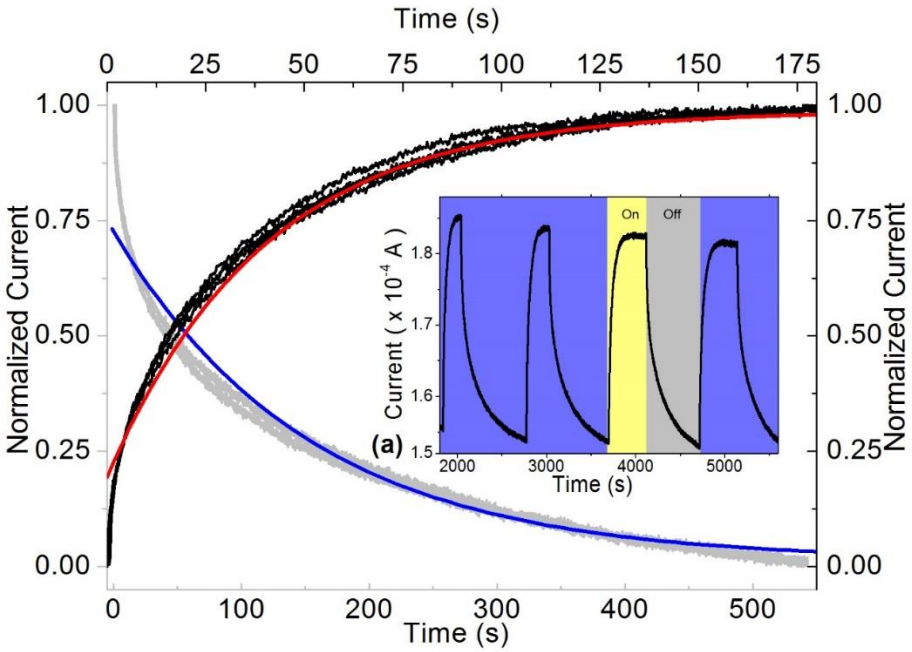

Figure 8.2 – Normalized currents for the four cycles ON/OFF represented in the inset picture (a) and respective fitting curves using the PPC model for the rise (red) and for the decay (blue) cycles using equations 8.9 and 8.10 respectively.

Fig. 8.2 shows the superposition of the four normalized On and Off cycles, where the current was normalized to the saturation value of each cycle for long irradiation times, as will be explained in detail further ahead.

An (*I-V)* curve was also measured for this sample to put in evidence details about the behavior of the sample conductivity when the voltage values changed. The constant current for values under -30 V and for values above 50 V, correspond to limitation of the current programed on the parametric analyzer in order to prevent damage of the samples due to Joule effect.

In figure 8.3 the measured *I-V* curves before (blue line), while exposed to (violet line) and after (light blue) UV irradiation are represented. The inset figure (a) represents the same results but represented in a logarithmic scale, in order to enhance the differences in the contacts as reported previously in chapter 5, as well the UV response of the device with and without UV.

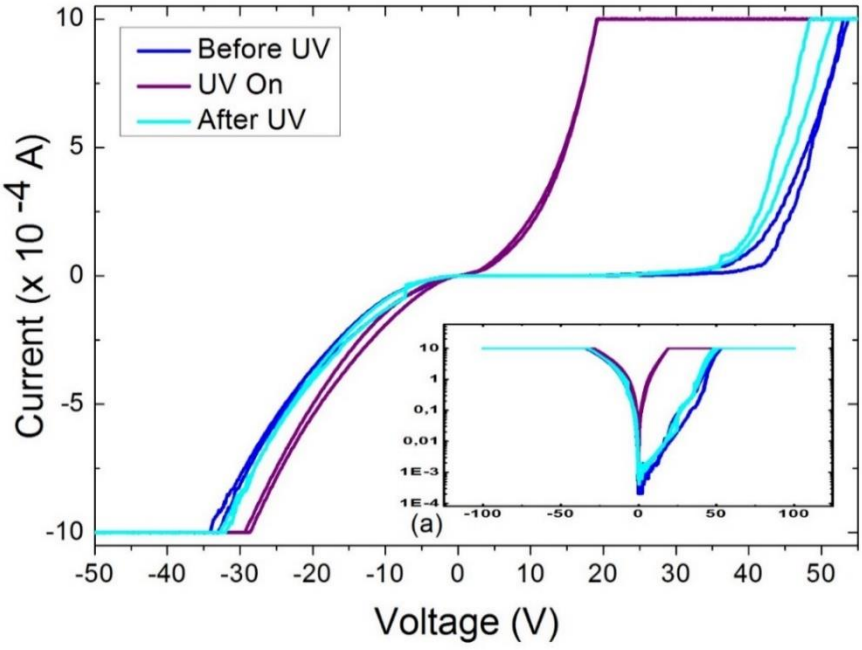

Figure 8.3 - *I-V* curves for β-Ga_2O_3 #1 flake before, during and after irradiation with UV light

It can be observed that the *I-V* curves before and after UV exposure were similar, being the difference between them concerned with the hysteresis mentioned in Chapter 5, but also having a clear superposition of the curves in the logarithmic scale before and after UV excitation, meaning the sample's characteristics were not changed. Under irradiation the *I-V* curve becomes quite symmetric with conduction thresholds –negative and positive – around -30 and 20 V. The resistance of the device was only momentously changed,

because when the UV light is turned OFF, the device returns to its original *I-V* characteristics.

8.3.2 Ga_2O_3 2D Proton Irradiation

The same Flake Ga_2O_3 (Table 5.1, Chapter 5) with silver contacts which was tested under UV irradiation, was then irradiated with the proton beam, for more than one hour (Fig. 8.4 (a)).

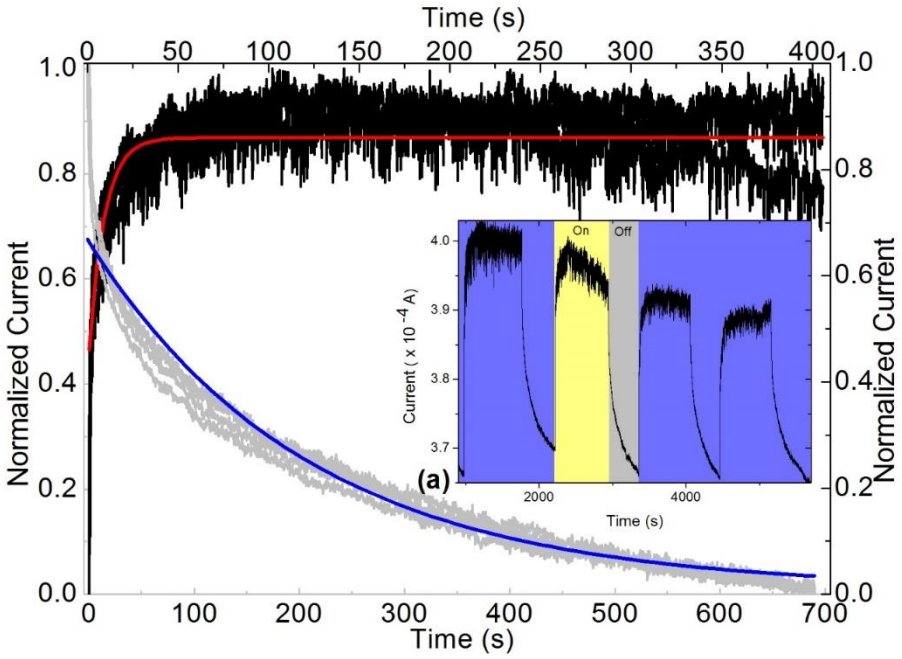

Figure 8.4 – Normalized *I(V)-t* curves for β-Ga_2O_3 #2 flake irradiated with a 2 MeV proton beam (a) inset picture correspondent to the in-situ measured current

In the inset of Fig. 8.4 the absolute *I(V)-t* plot for a constant voltage of -10 V can be observed, acquired while the sample was being irradiated (proton-ON) and the rest period after each irradiation (proton-OFF).

A decrease in the absolute value of the current can be observed in time, meaning the changes caused by the high energy beam are affecting the sample structure and creating defects.

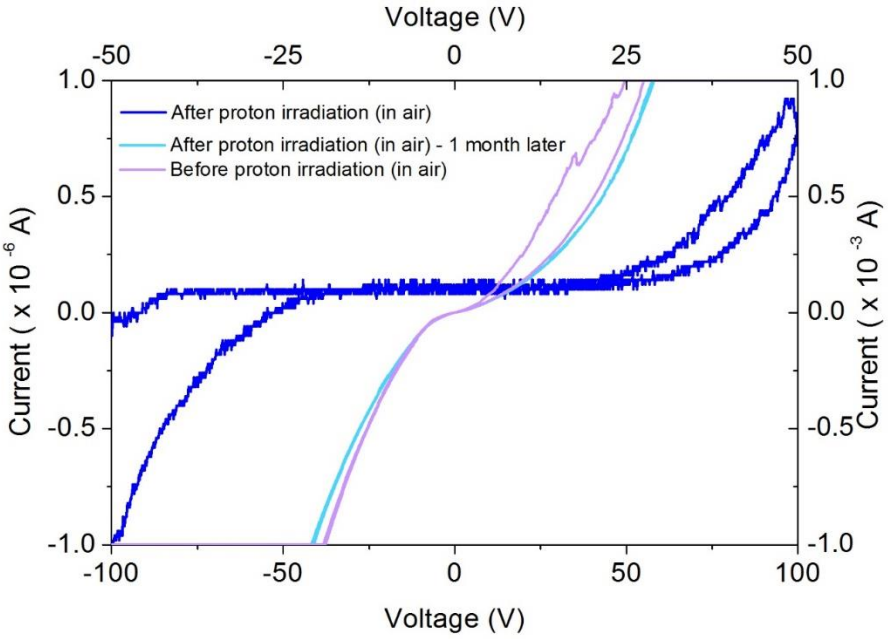

Figure 8.5 – *I-V* curves for β-Ga_2O_3 #2 flake irradiated with a 2 MeV proton beam.

Fig. 8.5 presents the *I-V* curves acquired before and after proton irradiation. Directly after the irradiation the electrical properties of the device are strongly degraded and conductivity is only obtained for very high applied voltages.

It is interesting to observe (Fig. 8.5) that one month after the sample had been irradiated, it recovered almost all of its initial conductivity, without any annealing, meaning the layers contributing to the conductivity recovered their charge density. The differences observed in the curves before and one month after irradiation may even not correspond to changes afflicted by the bombardment but may be associated with the hysteresis explained in Chapter 5.

This recovery might be related with the adsorption of the oxygen molecules at the surface of the device as discussed in Section 8.1.

8.3.3 Ga_2O_3 1D UV

The sample now analyzed is a gallium oxide nanowire doped with tin (Table 5.1, Chapter 5) and with silver contacts.

The current intensity, was measured, *in-situ,* using the parametric analyzer, for a constant applied voltage (-10V). The current intensity versus applied voltage (*I-V* curves) was measured and *I-V* curves are compared before and after irradiation and during UV excitation (Fig. 8.6), where the sample was totally irradiated with the UV light, using the same setup as used for the 2D flakes.

The background light was checked to not contribute to the conductivity of the device. Fig. 8.6 shows the *I-V* curves without light as well as during irradiation with visible or UV light.

Again no effect is seen for irradiation with visible light. This result can be observed in Fig. 8.6. The slight difference in evidence in the logarithm plot a), is not due to the influence of visible light but it is due to the hysteresis that sometimes takes place when two measurements are done one right after the other.

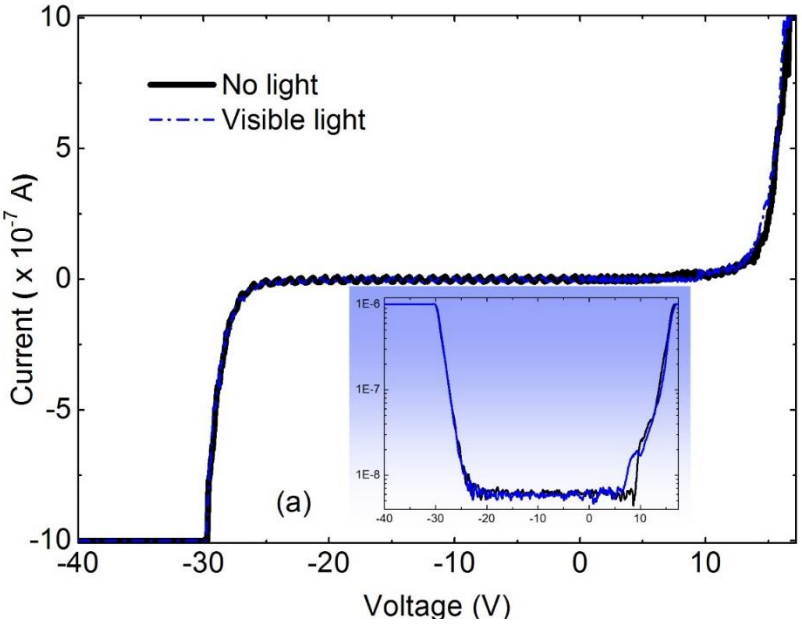

Figure 8.6 – *I-V* curves for the Sn-β-Ga_2O_3 nanowire irradiated with visible light.

The inset in Fig 8.7 represents the *I(V)-t* plot acquired during the UV irradiation and a steep increase of the current can be observed due to the photo-generated free charge carriers. The intensity of the current as a function of time, I (t), was measured for three cycles of light on (UV-ON) and off (UV-OFF).

It should be noted that at the time of this measurement, this sample had been already irradiated twice with a proton beam. This means that the sample might be already permanently affected in some way by the proton beam.

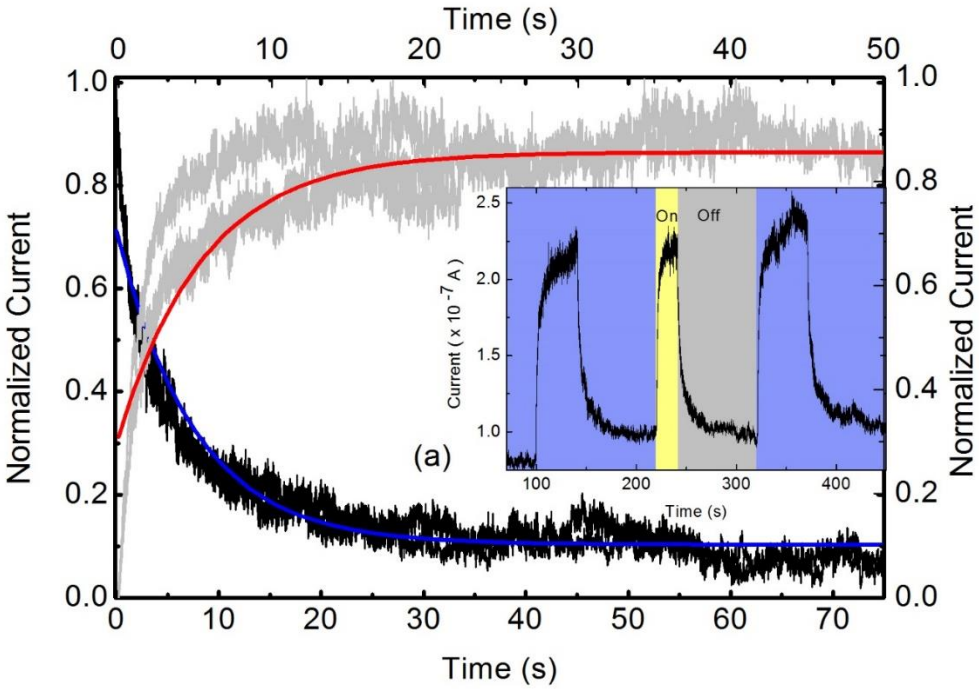

Figure 8.7 – *I(V)-t* curves for the Sn-β-Ga_2O_3 nanowire. Decay and rise times for the three cycles ON/OFF represented in the inset picture (a) and respective fitting curves using the PPC model for the rise (red) and for the decay (blue) cycles.

When the sample recovers from the period of excitement (OFF) persistent photo-conductivity phenomena can be observed The initial current value for the device is $I_t = 8 \times 10^{-8}$ A and when it is irradiated with UV light it increases up to $I_t = 2.25 \times 10^{-7}$ A.

Also it can be observed in the inset that the absolute value of the current is increasing in time, showing that the sample is accumulating charge, since with UV light no damages are being caused in the semiconductor.

8.3.4 Ga_2O_3 1D Proton Irradiation

The same nanowire tested in the previews section, was irradiated with protons of 2 MeV kinetic energy (Fig. 8.8 (a)).

This was the third time this sample was subjected to irradiation, and the initial abrupt decrease in the current that can be observed between 190 and 400 seconds of measurement, was not observed in the two first irradiation experiments, were the I(V)-t plots were much more stable and similar to that of Fig. 8.8 a), for the case of 2D flake proton irradiation.

Since the contacts were also being irradiated, this result of abrupt decay of the current, cannot be straightly attributed to the action of the beam in the sample. Further

studies, with new nanowires, would have to be performed in order to address the sensitivity of the sample to the irradiation.

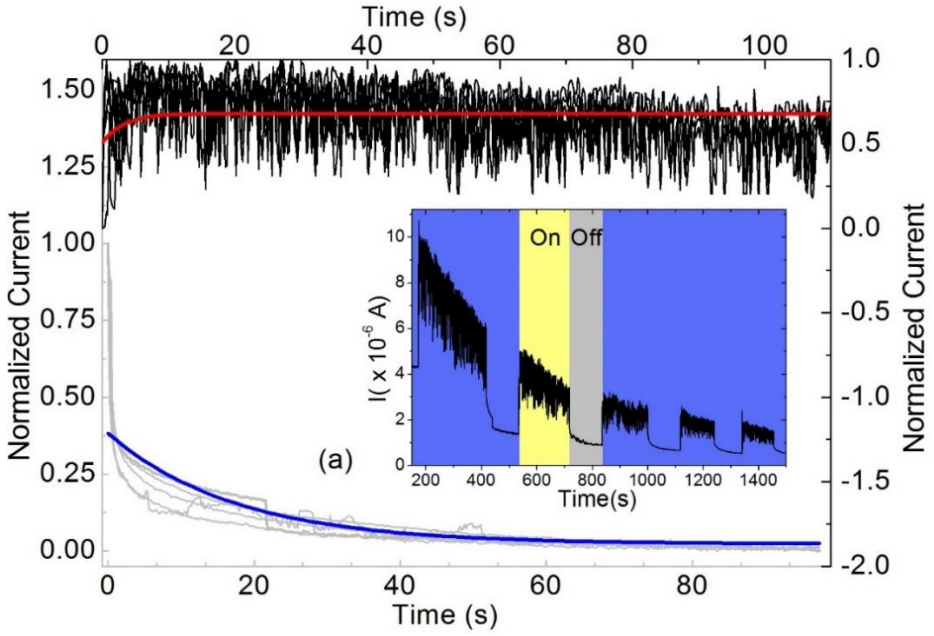

Figure 8.8 - *I(V)-t* curves for Sn-β-Ga_2O_3 nanowire irradiated with 2 MeV proton beam

The *I(V)-t* plot was measured for a constant voltage of 60 V, acquired while the sample being irradiated (proton-ON) and the rest period after each irradiation (proton-OFF). It was set a high tension of work, because the nanowire was responding in a rather irregular manner.

The currents are normalized from 0 to 1, but in order to bring all the information concerning this irradiation together, the scale representing the decay times (grey *y* scale), was extended to bigger values (1.5).

8.3.5 MoO_3 2D Flake UV

Molybdenum trioxide devices using flakes (2D) (Table 5.1, Chapter 5) with pure indium contacts, were obtained from bulk molybdenum trioxide (Chapter 3) and were exposed to UV radiation in air.

Using the tungsten/halogen lamp, the sample was exposed to visible and infrared light from 400 nm (3.1 eV) up to 1600 nm (0.78 eV), energies below the bandgap of MoO_3 (3.1 eV), and using the deuterium lamp UV, excitation above the bandgap was performed.

No effect on the samples conductivity was observed for excitation with light for this sample for either case.

This result can only be attributed to a bad contact, because in "the worst case scenario" assuming a perfect sample (with no defects), the UV light has enough energy to excite the electrons from the valence band to the conduction band.

Since these samples have defects caused by oxygen vacancies, a typical phenomenon of oxide semiconductors, they sure have energy levels inside the forbidden band, and even energies below 3.1 eV should be enough to influence the conductivity of the molybdenum trioxide flake with the lamp.

8.3.6 MoO_3 2D Flake Proton Irradiation

Particle Induced X-ray Emission maps were acquired from the molybdenum oxide during the irradiation of the sample with a 2 MeV proton beam.

The Molybdenum Lα1 and Kα1 lines 2D map are represented in Fig. 8.9. These maps allowed assuring the sample was being totally irradiated since this material does not emit in visible light like in the case of gallium oxide.

The detector is on the right side of the sample in this image that is why a shadow can be observed in the image correspondent to the Kα1 line of molybdenum oxide x-ray emission. A difference can be observed between the Kα1 line and the Lα1 line since the probability of absorption for the Kα1 line energy is higher than for Lα1 line.

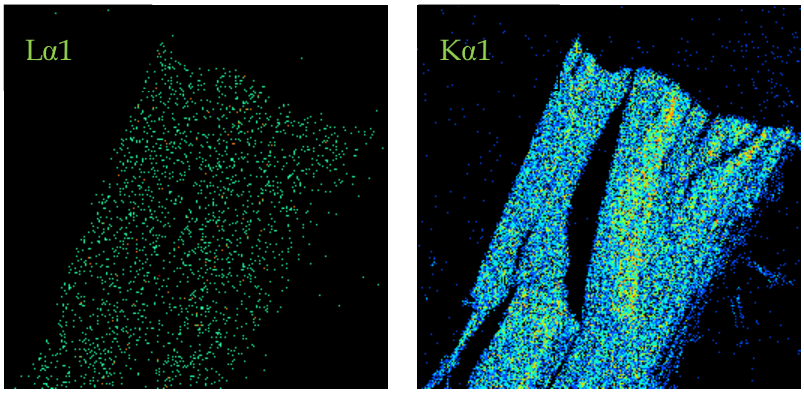

Figure 8.9 – PIXE images of MoO_3 flake (Table 5.1, Chapter 5) of the Lα1 and Kα1 X-ray lines of Molybdenum

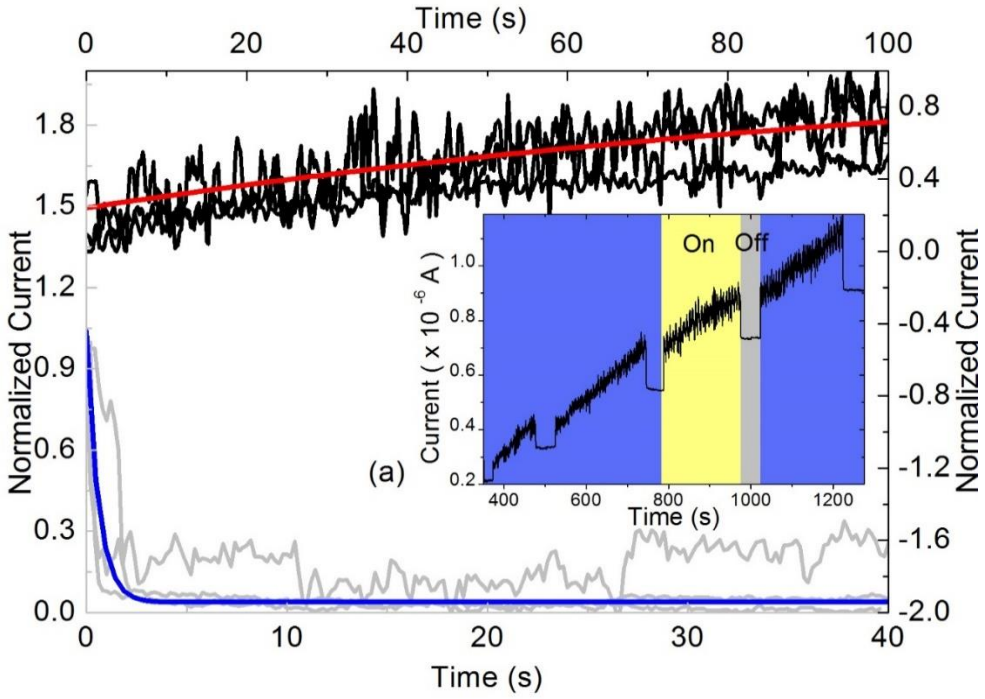

Figure 8.10 – I(V) -t curves for the MoO_3 flake irradiated with proton beam.

In the inset of Fig. 8.10 the absolute current as a function of time, I(t) plot, for a constant voltage of -10 V can be observed to have an increasing base value in time, which can be attributed to the beam and also to the charge accumulation of this wide band gap semiconductor. Since the same tendency was observed on the gallium oxide nanowire (section 8.3.4) this steep increase in the absolute values of the current in a short period of time (for 400 seconds the maximum current is $0.2 \times 10^{-6} A$ and for 1200 seconds the maximum current is $2 \times 10^{-6} A$), might be due to the effect of the high energy beam in samples with small thicknesses.

8.3.7 MoO_3 2D nanoplate UV

The sample now analyzed is a molybdenum trioxide nanoplate (Table 5.1, Chapter 5) with indium contacts.

The current intensity, was measured, *in-situ,* during UV-irradiation, using the parametric analyzer, for a constant applied voltage (-2 V).

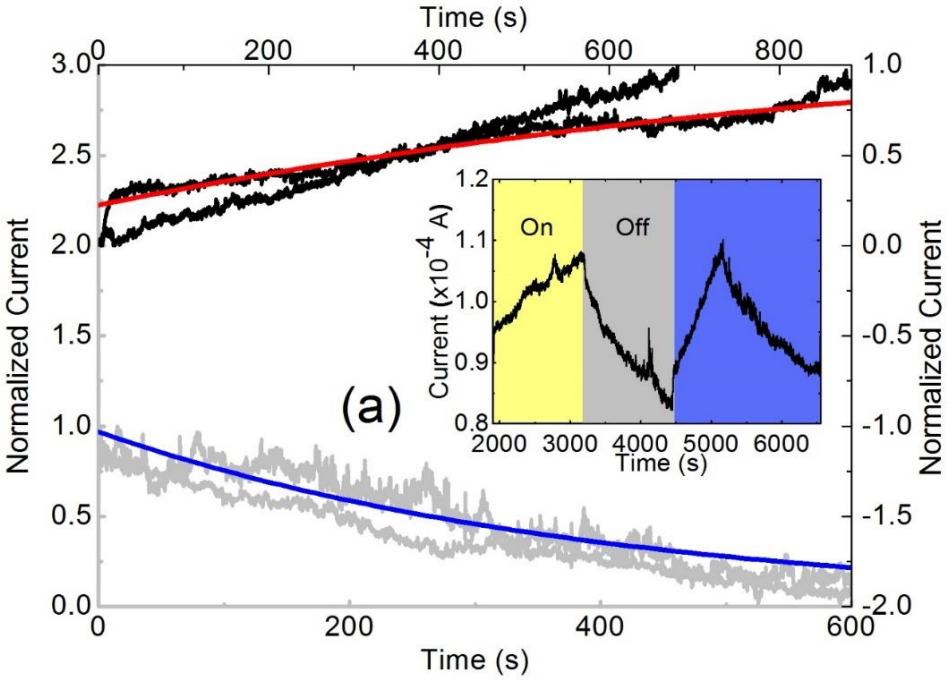

Figure 8.11 – Normalized currents for the two cycles of UV ON/OFF represented in the inset picture (a) and respective fitting curves using the PPC model for the rise (red) and for the decay (blue) cycles

In order to compare the sample before and after irradiated with the 2 MeV proton beam, UV measurements were carried out before (Fig. 8.11) and after the irradiation (Fig. 8.12).

The results were compared in order to address if the samples are being permanently changed by the beam. It is clear that the rise time after irradiation is almost the double than before the proton irradiation process.

Because this sample is small in overall dimensions and with 500 nm thickness this could mean that the beam permanently changed the sample's structure.

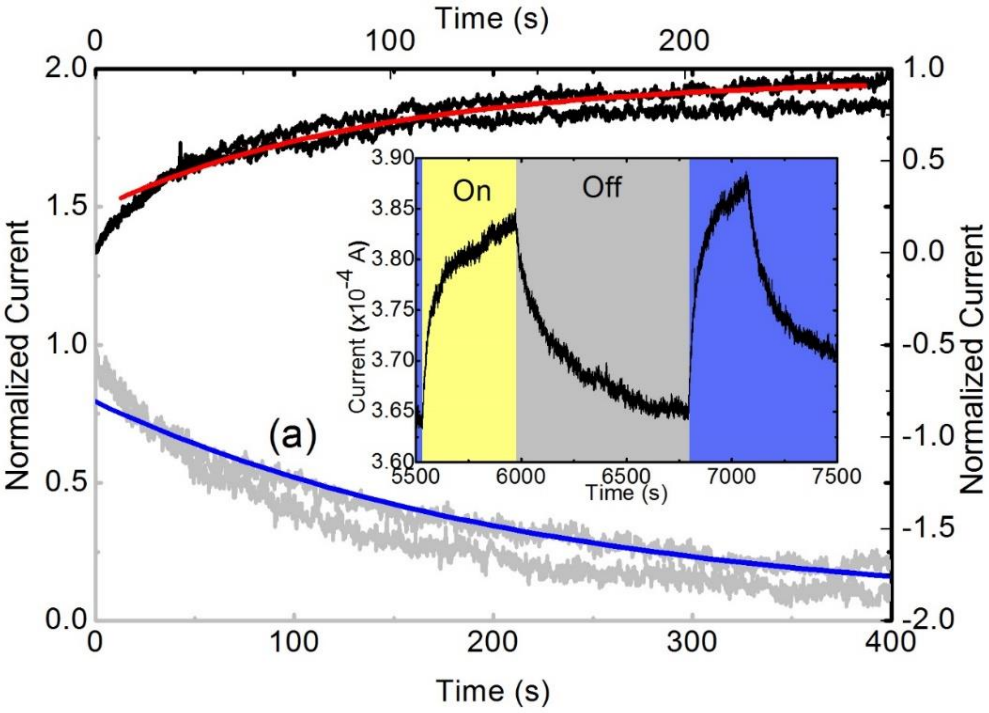

Figure 8.12 – MoO_3 nanoplate UV study after proton irradiation

8.3.8 MoO_3 2D nanoplate Proton Irradiation

Particle Induced X-ray Emission images were acquired from the molybdenum oxide sample during the irradiation of the sample with a 2 MeV proton beam.

The indium Lα1 lines 2D map are represented in Fig. 8.13. These maps allowed ensuring the sample was being totally irradiated since this material does not emit visible light like the case of gallium oxide. In this case, it was very difficult to obtain a good count of molybdenum and only by identifying the position of the sample on the device though indium x-rays, allowed to ensure the position of the sample on the chamber and verify if it was being totally irradiated.

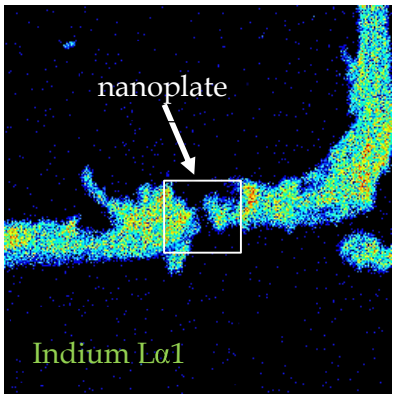

Figure 8.13 - PIXE map of MoO_3 nanoplate (Table 5.1, Chapter 5) of the Lα1 X-ray line of Indium

The sample was irradiated with protons of 2 MeV kinetic energy (Fig. 8.14 (a)).

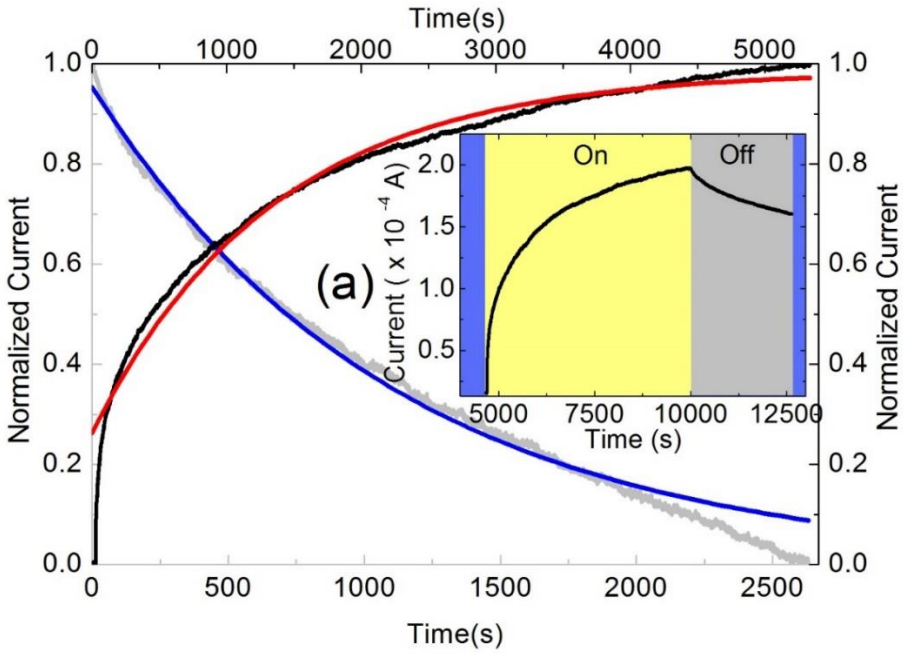

Figure 8.14 - *I(V)-t* curves for MoO_3 nanoplate irradiated with 2 MeV proton beam (a) inset picture correspondent to the in-situ measured current

As reported in Chapter 5, Table 5.1, this sample was produced on a sapphire substrate and sapphire when irradiated with the 2 MeV proton beam emits in the blue region. In order to address if the luminescence of sapphire excited the nanoplate, the conductivity of the nanoplate was measured while only sapphire was being irradiated.

Fig. 8.15 shows the *I(V)–t* plot of the sample while only sapphire was being irradiated. Each On represented the times where the beam was upon sapphire and as can be observed the current intensity is always decaying (it is decaying because the nanoplate had been previously irradiated with the 2 MeV proton beam) and even for the longer excitation period (between 1600 and 2300 seconds) the conductivity continues to decrease. The effect of sapphire ion-luminescence is therefore negligible.

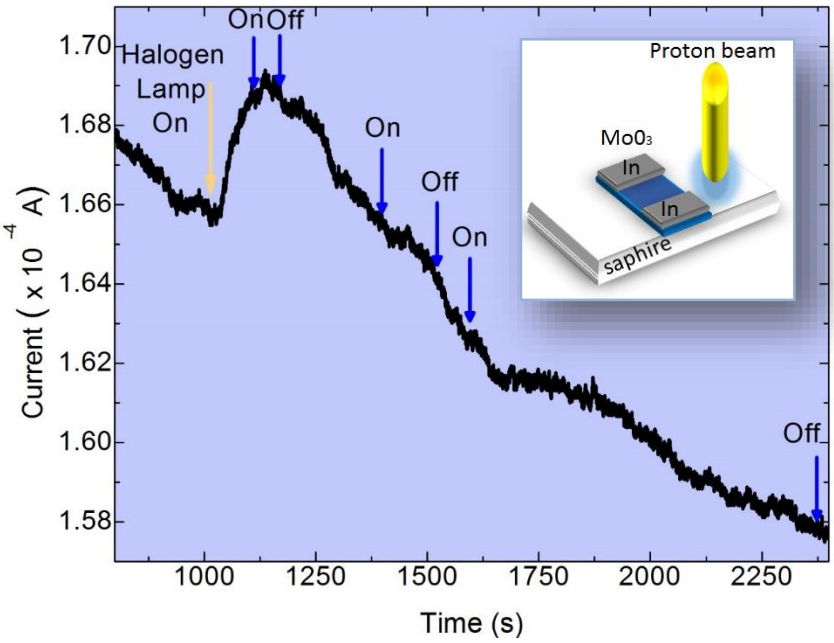

Figure 8.15 – I(V) –t test of the influence of the luminescence of sapphire on the molybdenum trioxide sample

In constrast to measurements done in air with the High Power UV-Vis Fiber Light Source, L10290, where the sample did not show any response when irradiated with visible light, in vacuum whenever the Halogen Lamp inside the chamber (Chapter 4) was turned On, the sample suffered an increase in its conductivity, as was expected and discussed (see section 8.3.5).

8.4 Photo induced (UV) persistent conductivity. Discussion.

All the semiconductor oxides in study present an increase in conductivity when excited with ultraviolet light as well as persistent currents when the excitation light is switched off. As discussed in Section 8.1, the confinement of free charge carriers due to surface band bending, caused by the adsorption of O_2 molecules that act as electron traps represents one model to explain this persistent current.

So in the following section the results obtained in Section 8.3 are going to be analyzed taking into account that this is the phenomena behind the PPC for both materials in study.

8.4.1 Ga_2O_3 2D

Regarding the results obtained for the *I-V* curves (Fig. 8.3) and in order to understand the physical principles behind the different trends observed for the *I-V* curves, a scheme of the electrical circuit and energy diagrams caused by the contact between metal and the semiconductor was made (see Fig. 8.16).

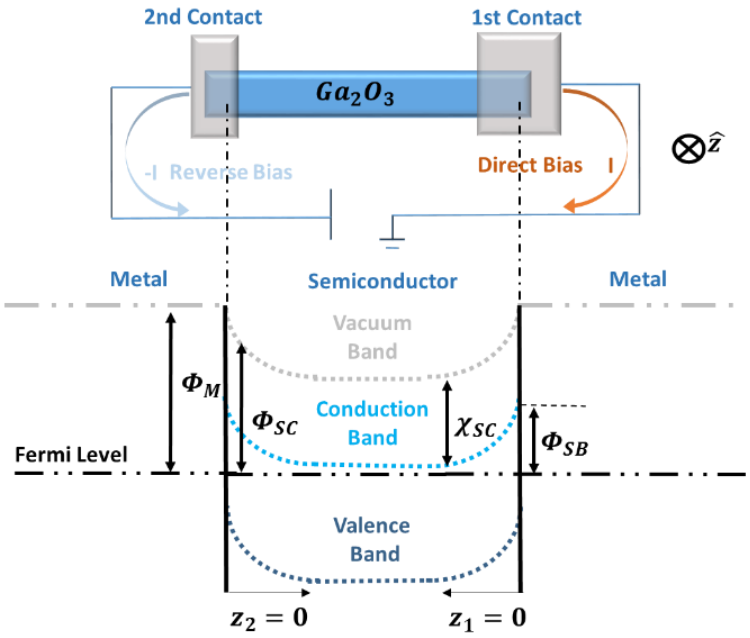

Figure 8.16 - Scheme of the electric circuit studied and the correspondent one-dimensional junction scheme without any UV light present.

The curve presented in Fig. 8.3 is clearly asymmetric so it can be assumed that the Schottky barrier heights are different in the two contacts, as explained in chapter 5. The stronger photoconductivity effect is seen for the contact that shows a higher resistivity in reverse bias. It is therefore assumed that the depletion layer formed at this contact is larger and that the influence of photo generated charge carriers is higher than for the lower resistivity contact.

The I(t) result indicates that:

a) the material is sensitive to UV light, even in the segment of the plot where the effect was less noticeable in the IV plot and;

b) the persistent conductivity is observed, after switching off the UV excitation where the base current during radiation increases approximately 20%, to a maximum value of 1.8×10^{-4} mA.

Regarding the I(t) plot for UV test the buildup and decay transients of the photo-current follow non-exponential time dependence as reported in Chapter 8.1. The Kohl-rausch stretched exponential analysis will be used to do the data treatment of both UV and proton plots.

Applying the stretched exponential function two parameters have to be determined: the time constant τ and the value for γ.

Since fitting the rise and decay curves with equations 8.9 and 8.10 did not allow to determine the values of both variables with confidence the following approach was followed. As can be observed in the insets in all UV and proton plots, the device response follows a tendency that can be treated as a 1st order system approximation [46]. Therefore, one variable, the τ, was taken directly from the normalized curves and the γ value can be determined fitting equations 8.9 and 8.10 with this time constant.

The first order systems characteristics can be determined calculating the solutions of differential equation of the system [46].

Figure 8.17 - Scheme representing the input function, *Iconstant(t)*, the S (representing the response of the device) and *I(t)*, the output function

The transference function of the material, G(s), can be calculated regarding the Laplace transform of the input, $\mathbf{I}_{\mathbf{constant}}(t)$ ($\mathbf{I}_{\mathbf{constant}}(s)$) and the output, i(t) (I(S)) (see Fig.8.17), since the time is removed from the equations, and the time dependent function can be calculated by inverting the Laplace function. For instance, if the input, $I_{constant}(t)$ is an invariant step function in time and the output I(t), is an exponential function the transference function, G(s), is given by:

$$G(s) = \frac{a}{bs + c} \tag{8.11}$$

Therefore

$$\frac{I(s)}{\mathrm{I_{constant}(s)}} = \frac{a}{bs + c} = \frac{\frac{a}{c}}{\frac{bs + c}{c}} = \frac{\frac{a}{c}}{\left(\frac{b}{c}\right)s + 1} \tag{8.12}$$

Where $\frac{a}{c}$ is the system gain,K_0, and $\frac{b}{s}$ is the time constant of the system, τ. So, knowing the input and output functions of the system, under the boundary conditions (i.e., invariance in time), the time constant can be determined. Substituting in the original equation:

$$\frac{I(s)}{\mathrm{I_{constant}(s)}} = \frac{K_0}{\tau s + 1} \tag{8.13}$$

Where the output, $I(s)$, is calculated and inverted (equation 8.13) giving the variation in time of the output function:

$$I(s) = \frac{K_0}{\tau s + 1} \cdot \frac{1}{s} = \frac{K_0}{s} - \frac{K_0 T}{(Ts + 1)} \tag{8.14}$$

and

$$I(t) = \mathcal{L}^{-1}[I(S)] \tag{8.15}$$

The PPC output plots present an answer of first order type. This is a typical approach in order to determine directly from the plot the value of the time constant if I(t) is at 63.2% of its initial value, for example. The ON times are described by the Output function and the OFF times are described by the Symmetric Output function as referred in Chapter 8.1. In this sense, the time response of the system is given by:

Table 3 - First Order Response output function

Time constant, $\boldsymbol{\tau}$	Output function	Symmetric Output function
t=$\boldsymbol{\tau}$	$K_0(1-e^{-1})$ =0.632 K_0	$1-[K_0(1-e^{-1})] = 0.368\ K_0$
t=$\mathbf{5}\boldsymbol{\tau}$	$K_0(1-e^{-5})$ =0.993 K_0	0.007 K_0

Using the expression found in Table 3, the time constant for the rise and decay can be determined directly from the plot in study as exemplified in Fig. 8.18.

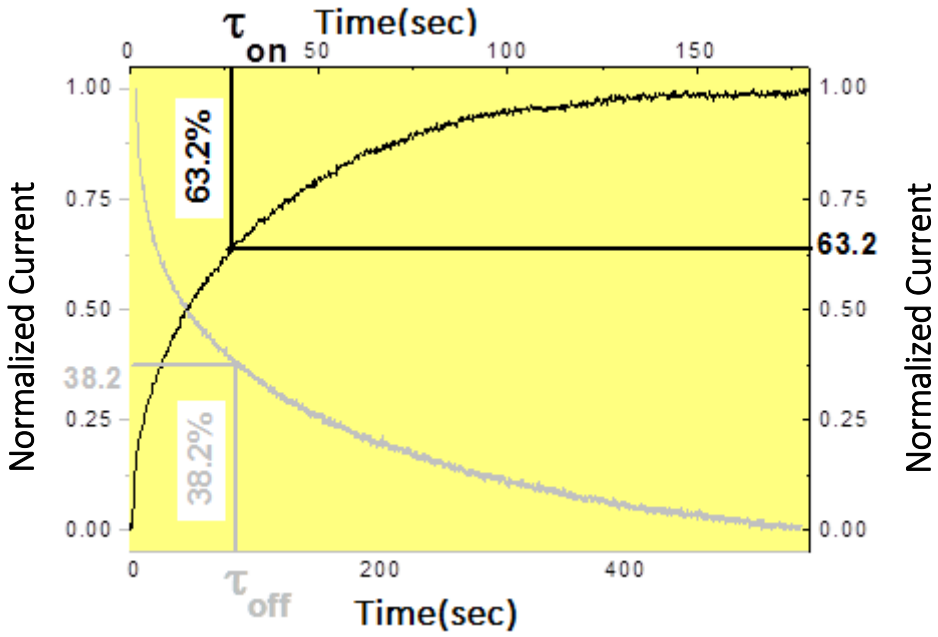

Figure 8.18 – *I(V)-t* plot for one normalized rise(black) and one decay(grey) curve for the 2D Ga_2O_3UV in order to determine respectively both τ_{On} and τ_{Off} when the current is 63.2% or 38.2% of the initial value.

In order to obtain the correct value for τ it is necessary to normalize the *I(V)-t* curves because the input function is not equal to unity and in order to enable a meaningful comparison between the results obtained in each measurement.

For that purpose, a normalization to the maximum intensity was done and before the normalization each curve was shifted in time in a way that the initial instant (t= 0 s) was chosen to be the instant when the light was switched on/off. Then for all the current values belonging to one curve, the normalization was made using the following formula:

$$I' = \frac{I - I_{min}}{I_{max} - I_{min}}. \qquad (8.16)$$

In Table 4 are shown the results obtained for determining the time constants for the *I(V)-t* plot for the UV irradiation of the gallium oxide flake.

Table 4 - Time constants for rise and decay of the plot in Fig. 8.2

UV Cycle	τ_{ON} (s)	τ_{OFF} (s)
1st	27.71	82.20
2nd	28.20	89.00
3rd	27.95	95.40
4th	30.37	101.40
Mean Value	28.56	92.00

Using the PPC model fitting (equations 8.9 (rise) and 8.10(decay) in section 8.1) and fixing the values for the time constants obtained in Table 4, it is now possible to determine the values of γ and respective uncertainty. The values correspondent to the UV excitation of gallium oxide flake are represented in the table 5 with corresponding correlation coefficient $r^2$of the fit.

Table 5 - Values of γ from the fit with PPC model, for each cycle

UV Cycle	γ_{on}	γ_{Off}
1st	0.81	0.54
2nd	0.75	0.67
3rd	0.77	0.69
4th	0.75	0.71
Mean Value	0.77 ± 0.02	0.65 ± 0.06

As can be observed (Fig. 8.4), for consecutive cycles the answers of the material are similar when irradiated with UV light as expected because, in principle, with UV excitation, no defects are being produced. The mean values of γ for ON and OFF were calcu-

lated and showed that the values stay closely the same for each case for successive measurements. It is expected that the density of defects contributing for the PPC for each ON\OFF cycle remain the same. A good reproducibility was achieved although the conditions were not ideal for measuring photoconductivity (the measurements were done in air and the samples were always exposed to possible contaminations from the laboratory, even though, exfoliation should provide clean crystal layers).

Also, for decay and rise times, there are different densities of defects contributing for the persistent photoconductivity where $\overline{\gamma_{on}} = 0.77 \pm 0.02$ and $\overline{\gamma_{off}} = 0.65 \pm 0.06$. This could be expectable since with UV ON the process of removal of molecules adsorbed on the semiconductor surface is quicker and the production of free charge carriers involves a lot of mechanisms and recombination's in between, as for example, meanwhile a molecule of oxygen is being desorbed from the surface with the energy provided by the UV light at the same time molecules are again being adsorbed once it's exposed in air. As for the case of UV OFF, it shows that the adsorption of the oxygen molecules is happening in a slower rate, also observed in the decay constant time of 92 seconds calculated in Table 4, and causing the same surface states to contribute for the PC with similar energies behind them.

8.4.2 Ga_2O_3 1D UV

For the nanowire device, regarding the results obtained for the *I-V* curves (Fig. 8.6), the same logic applied as for the case of the flake in terms of contact response to the UV excitation (see Fig. 8.16, Section 8.4.1) and the asymmetry is once again attributed to the different depletion zones between the semiconductor and the metal from both contacts.

The I (t) (see Fig. 8.7) result indicates once again the material's response to UV light and the persistency in conductivity is once again observed.

The time constant τ and the value for γ will be calculated in the same way that it was done for the gallium flake.

This device had already been irradiated with the 2 MeV proton beam before this UV measurement.

Table 6 - Time constants for rise and decay of the plot in Fig. 8.7

UV Cycle	τ_{ON} (s)	τ_{OFF} (s)
1st	1.98	3.80
2nd	3.01	4.26
3rd	4.80	5.8
Mean Value	3.26	4.62

The values for the PPC model are described in the Table 8.5.

Table 7 -Values of γ from the fit with PPC model, for each cycle in Fig. 8.7

Measurements	γ_{on}	γ_{Off}
1	0.35	0.53
2	1.0	0.68
3	0.86	0.76
Mean Value	0.73 ± 0.27	0.66 ± 0.09

The mean values of γ for ON are irregular and a mean value might not be the most correct approximation to do, considering that this was an already irradiated sample and the effect of two irradiations caused permanent changes (the nanowire emitted blue light in the two first proton irradiation tests and quit emitting after the last one was performed [no luminescence plots were taken and ,so, the results are not shown in this work]) and since the working conditions are not perfect (the optical fiber was sustained manually in this measurement (contrary of the case for the gallium oxide flake and for the molybdenum samples, that a support for the probe was used) the way that the sample was excited does not allow a correct interpretation of the values of the γ parameter. In fact, looking for the stable results observed for the Off periods, with $\overline{\gamma_{off}} = 0.73$, it probably demonstrates that the defects contributing for these PPC results are similar in terms of energy and similar to those obtained for the gallium flake ($\overline{\gamma_{off}} = 0.66$)

8.4.3 MoO_3 2D Flake UV

This flake of molybdenum trioxide did not show any response for UV excitation or visible light. This was not an expected result since this semiconductor has a band gap of 3.1 eV, and having the lamp energies that go from 6.2 to 0.78 eV and being this material sim-

ilar with the gallium oxide one in terms of crystal structure (both are oxide semiconductors in the 2D limit), and having gallium oxide a larger band gap (4.8 eV) this probably means that the very high brittleness of these crystals are behind the poor quality of contacts, that are probably too resistive, turning this device insensitive to UV light.

8.4.4 MoO_3 2D Nanoplate UV

Contrary to the results acquired for the flake, the nanoplate did respond to UV excitation.

Since this was the last device produced for this work, and having been the others first experiments either for contacts production, for UV excitation and proton irradiation evaluation, some steps were fulfilled this time in order to address the changes made by irradiating the samples. Namely, the sample was excited with UV light, before and after being irradiated with the proton beam, and differences in the *I(V)-t* plots were evaluated.

The UV study was performed in the same conditions for both measurements.

The Tables 8.6 and 8.7 contain the results of the $\boldsymbol{\tau}$ calculated for Fig. 8.11 and Fig. 8.12, correspondent to the *I(V)-t* plots before and after proton irradiation, that where treated in Section 8.3.7

Table 8 and Table 9 – Values of τ from the fit with PPC model, for each cycle in Fig. 8.11 and 8.12 respectively.

UV Cycle (BEFORE)	$\boldsymbol{\tau_{ON}}$ (s)	$\boldsymbol{\tau_{OFF}}$ (s)	UV Cycle (AFTER)	$\boldsymbol{\tau_{ON}}$ (s)	$\boldsymbol{\tau_{OFF}}$ (s)
1st	422	242	1st	58,8	110
2nd	445	401	2nd	91,6	160
Mean Value	433.5	321.5	Mean Value	75.2	135

It can be observed that this sample before it had been irradiated had the biggest time constant from all the samples studied, for both rise and decay times, and after it had been irradiated the decay constants become approximately half of the value measured before for the case of OFF and around a fourth of the value measured for ON periods.

Comparing these values of the time constant with the values obtained by the Kohlrausch stretched exponential, as has been done in the previews analysis, it can be observed that for the periods where the sample is being irradiated with UV, the $\boldsymbol{\gamma_{on}}$ values suffer great changes after the sample had been irradiated, changing from a mean value of 0.2 to a mean value of 0.80 (see Tables 10 and 11).

This could mean that the defects contributing for the persistent current might be largely different before and after the proton irradiation, and the defects that are contributing for the PPC effect before proton irradiation possibly have a larger recombination time causing the large constant time.

Once again the γ_{Off} values are larger for the decay period than for the rise period and a resemblance can be observed between these results and those obtained for the gallium oxide devices.

Table 10- UV test for MoO_3 nanoplate before proton irradiation

Measurements	γ_{on}	γ_{Off}
1	0.39	0.79
2	0.01	0.90
Mean Value	0.2 ± 0.19	0.84 ± 0.05

Table 11- UV test for MoO3 nanoplate after proton irradiation

Measurements	γ_{on}	γ_{Off}
1	0.63716	0.49
2	1	1
Mean Value	0.80 ± 0.18	0.75 ± 0.26

8.5 **Proton-Ion induced persistent conductivity. Discussion**

There is a major difference between exciting with UV and irradiating with ion beam: the last one is damaging the materials structure.

This fact was attested mainly by the gallium oxide samples, because they started emitting (ion luminescence) blue light and after some hours they stopped emitting, showing clearly that major changes are being done to the semiconductor crystal structure.

If those defects trap free charge carriers this means that some decrease in base conductivity will be measured with time as well. However, our measurements showed that this effect is not nearly as fast as the fading of the emission.

Light emission needs to present some intensity in order to be seen, and it comes from constructive interference of all depth of the crystal structure and although the beam

makes most of the nuclear collisions around 20 micrometers for both materials, it shows that in the electronic regime it is also causing major effects, changing the charge density of the crystal structure and changing the crystal potential.In all the setups in study, all the surface of the samples was irradiated with a uniform beam intensity (approximately).

8.5.1 Ga_2O_3 2D proton

The sample was irradiated with the proton beam around 1000 seconds for each cycle. In Table 12 it can be observed that the rise times are increasing with the increasing fluence of protons. In this sample a higher time constant is being associated with more defects. As for the case of the decay time, it can be observed that the same effect is happening.

Table 12 – Proton Induced Conductivity constant time for 2D gallium oxide flake correspondent to Fig. 8.4

UV Cycle (BEFORE)	τ_{ON} (s)	τ_{OFF} (s)
1st	3.2	50.2
2nd	3.8	58.8
3rd	7.8	65.4
4th	14.8	69.4

The Kohlrausch stretched exponential was applied, as has been done in the previews analysis for the UV experiment, and a comparison was tried to be made in order to compare both experiments in terms of conductivity effects.

The same first order treatment was applied to the proton plots, as was done for the UV case. In Table 13 the results of the stretched exponential are summarized.

Table 13 – Proton Induced Conductivity parameters for 2D gallium oxide flake of Fig. 8.4

Measurements	γ_{on}	γ_{off}
1st	0.3	0.4
2nd	0.2	0.5
3rd	0.4	0.5
4th	0.5	0.5
Mean Value	0.35 ± 0.11	0.48 ± 0.04

As can be observed in Fig. 8.4, the fitting done is not able to include the first and really abrupt increase in current. But in terms of the slower decay the fit was properly done.

It is expected that the parameter γ does not change greatly in this experiment, since it seems that only the first few nanometers of the gallium oxide flake are contributing for the conductivity of the device (see Fig. 5.11) and as observed in the TRIM simulations (Chapter 6.4, Fig. 6.6) the ionization profile and the damage profile show that both ionization and vacancy formation are more intense closer to the Bragg peak, which is at 22 micrometers in gallium oxide, meaning that the material is not suffering many changes whether by changing its charge, or whether by being damaged, and so, the amount of defects contributing for the persistent current is almost the same.

8.5.2 Ga_2O_3 1D

The sample was irradiated with the proton beam around 250 seconds for each cycle.

As can be observed in Fig. 8.8 there is a large amount of noise in the measurement whenever the proton beam is irradiating the sample. Since this was not the first irradiation of this nanowire and it had already been irradiated two other times, a larger voltage of -60 V was needed to be applied for the *I(V)-t* measurement.

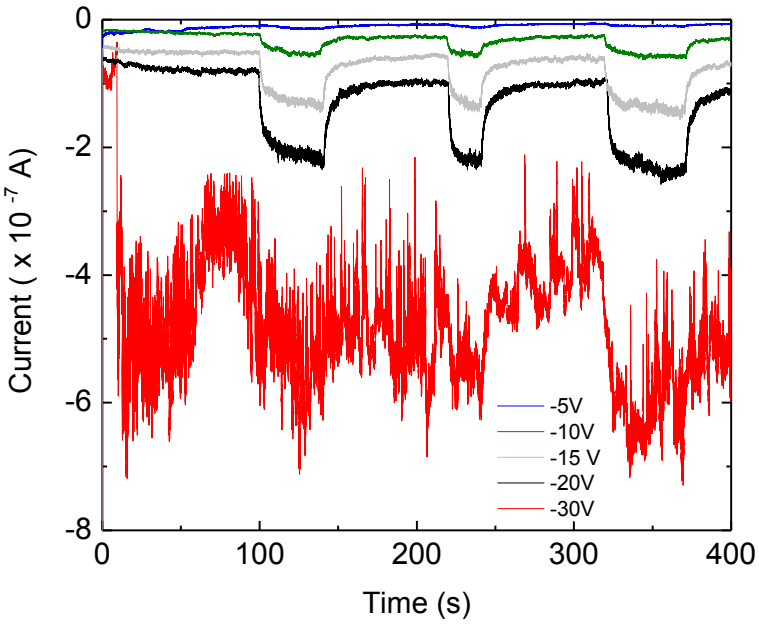

Figure 8.19 – *I(V)-t* plots for nanowire UV test for different voltage values

As can be observed in Fig. 8.19, showing a study of the influence of voltage to UV response, for voltages above 20V the noise in the measurement is greatly increased.

Table 14 – Proton Induced Conductivity time constant for 1D gallium oxide nanowire correspondent to Fig. 8.8

UV Cycle (BEFORE)	τ_{ON} (s)	τ_{OFF} (s)
1st	0.8	0.4
2nd	1.2	0,58
3rd	1.8	0,6
4th	3.2	1,2
5th	4.01	1,8

In Table 14 can be observed that the rise times are increasing with the increasing fluence of protons. In this sample a higher time constant is being associated with more defects.

In the case of the gallium oxide flake the γ parameter is almost the same throughout the irradiations (see Table 13), and in the case of the nanowire the changes are clear for the γ parameter.

For the Beam On cycles, although the fitting was reasonably good, it once again failed to address all the stages of the stretched exponential curve, and the amount of different defects contributing for the conductivity seems to be one dominant effect (equal to 1), showing that for the case where the beam has a strong electronic interaction and the sample is of the order of nanometers, the effects caused by irradiation are much more pronounced.

Table 15 – Proton Induced Conductivity parameters for 1D gallium oxide nanowire correspondent to Fig. 8.8

Measurements	γ_{on}	γ_{Off}
1st	1	0.05
2nd	1	0.04
3rd	0.97453	0.4
4th	1	0.13
Mean Value	0.99 ± 0.01	0.155 ± 0.145

8.5.3 MoO_3 2D flake

Table 16 shows the rise and decay time constants corresponding to the proton irradiation of a molybdenum trioxide flake.

Since this sample was not subjected to the same time of irradiation between cycles (Beam On /Beam OFF) as can be seen in Fig. 8.10 where the second cycle of irradiation (between 500 and 800 seconds), that correspond to the 1st measurement in Table 16, was greater than the other cycles studied.

That might be the reason, in terms of charge accumulation, for causing the second cycle to have such different values (approximately the double) for both constant times.

Table 16 – Proton Induced Conductivity time constants for a 2D molybdenum trioxide flake correspondent to Fig. 8.10

UV Cycle (BEFORE)	τ_{ON} (s)	τ_{OFF} (s)
1st	78.77	0.37
2nd	145.49	1.7
3rd	75.87	0.59

In Table 17 the results of the stretched exponential fit are summarized.

Table 17 – Proton Induced Conductivity parameters for 2D molybdenum trioxide flake correspondent to Fig. 8.10

Measurements	γ_{on}	γ_{off}
1st	1	1
2nd	0.7	1
3rd	0.6	1
Mean Value	0.087 ± 0.7	1

As can be observed in Fig. 8.10, the fitting done is not able to fully adjust the On/Off cycles and the values obtained for γ are not totally reliable, however some comparisons can be made.

It can be observed that the material is not suffering many alterations in terms of the surface contribution for the conductivity. This is related with the Bragg Peak, which is at

30.5 micrometers in molybdenum oxide bulk, and observing the irradiation profiles done with TRIM (Chapter 6.4, Fig. 6.7 and Fig. 6.8), the major effects in terms of permanent displacements of the crystal structure are proven to be mainly around the Bragg Peak.

It is expected that the parameter γ it is not changing greatly in this experiment a fact that can be observed by the inset (a), in Fig.8.10 where the conductivity stays practically the same.

8.5.4 MoO_3 2D nanoplate

This device proved to be the one to have the largest time constants for both On and Off cycle, as it had been already verified in the UV tests studied in Section 8.4.4, with values presented in Table 18.

Table 18 – Values of τ from the fit with PPC model, for Fig. 8.14

UV Cycle	τ_{ON} (s)	τ_{OFF} (s)
1st	441.43	1106.49

Particularly, after the sample was irradiated with the 2 MeV proton beam, the amount of different defects that contributed for the persistent conductivity increase, showing clearly that even though this sample had a width of 500 nm, and way shorter than the 30.5 micrometer of the Bragg Peak, the effects caused by electronic interactions are a major cause for changing the materials properties.

Table 19– proton irradiation for MoO_3 for Fig. 8.14

Measurements	γ_{on}	γ_{off}
1	1	0.79

8.5.5 Devices ON/OFF current Ratios to UV and Proton Irradiation. Thickness relation

Because of a sense of similarity between the dimensions of the samples and their response when being irradiated with the proton beam and UV light was being observed for both materials, the On/Off ratios between the maximum and minimum current that each device achieved was calculated.

In order to compare, the most stable cycle of each plot (for both UV and Proton tests) was chosen and the results are represented in Table 20.

Table 20– ON/OFF, OFF/ON Ratios for all the devices

			UV	Proton
			ON/OFF	ON/OFF
Ga_2O_3	Flake	Max	1.84E-04	3.93E-04
		Min	1.54E-04	3.63E-04
		Ratio	1.19	1.08
		Fig.	(8.2)	(8.4)
	Nanowire	Max	2.24E-07	1.80E-06
		Min	8.12E-08	6.62E-07
		Ratio	2.75	2.72
		Fig.	(8.7)	(8.8)
MoO_3	Flake	Max		9.10E-07
		Min		5.30E-07
		Ratio		1.72
		Fig.		(8.10)
	Nanoplate	Max	3.85E-04	1.90E-04
		Min	3.63E-04	3.00E-05
		Ratio	1.06	6.33
		Fig.	(8.12)	(8.14)
		Max	1.1E-04	
		Min	8.2E-05	
		Ratio	1.34	
		Fig.	(8.11)	

The correspondent figures from where the ratios were calculated are referenced for each sample and correspondent study. For instance, the maximum and minimum current for the UV test of the gallium oxide flake were taken from Fig. 8.2.

It is clear that for the smaller samples, as is the case of the gallium oxide nanowire and the molybdenum trioxide nanoplate, the response to proton irradiation is much bigger than for the case of the flakes. In fact, if the nanoplate was left being irradiated more time with UV light, it probably would show greater increase in current for both before and after irradiation with protons.

The larger response of the nanostructures is due to their larger surface/volume ratio, a greater surface is available for more adsorbed oxygen molecules or other surface effects, as was reported for the case of zinc oxide based devices [40].

9

Conclusions and future work

This Chapter will give two different discussions: First the conclusions concerning the actual results obtained throughout the experimental research will be summarized. Second, because this was the first time this kind of experiments were made in the group, a type of a step-by-step guide will be provided in order to help to perform measurements in an optimized way in the future.

One of the main goals for this work was to produce stable contacts that allowed reproducible electrical measurements, in order to evaluate the electrical response of two novel monocrystalline semiconductor oxides, Gallium Oxide and Molybdenum Trioxide, as radiation sensors.

Many metals were tested for contact production and their quality to perform good contact with the semiconductors in study was evaluated. Indium proved to be excellent for molybdenum oxide samples and silver ink proved to make the best contacts for gallium oxide samples.

In order to achieve such stable contacts many attempts were made using rapid thermal annealing processes, annealing in air and thermal evaporation. Although contacts produced by thermal evaporation are easily in the nanoscale order, for the crystalline structures used in this thesis, with high levels of brittleness, they prove to fail in keeping the device strong enough to be transported and mounted in the irradiation chamber, because these crystals are easily damaged and all considerations can be lost if they are scratched or broken. Annealing in air also proved to be inadequate because thin layers of oxygen are growing on the metal contacts during the annealing and they are known for being insulating layers.

RTA processes in vacuum or in argon ambient proved to be equally efficient, where the temperature proved to be good in two different ways: it melted the metals allowing better contact to the rough surfaces and better adherence and, possibly, the occurrence of diffusion.

Since the silver ink is a polymeric paint, the annealing of the sample should be performed prior to making the contacts or it will evaporate.

Metal-Semiconductor-Metal was found to be the better configuration for the test devices. The characteristic *I-V* curves obtained for these devices are of back-to-back Schottky type.

Insulator substrates that resist both to temperatures up to 300 ^{o}C and proton beam irradiation and that proved to not influence the conductivity of the materials or the measurement itself were tested. Kapton tape was the best material for this purpose and also it allowed to produce samples of few micrometers by mechanical exfoliation, having made samples for irradiation studies with thickness of 10 μm, without them losing their crystalline structure.

For gallium oxide samples, the better configuration for electrical contacts is along the b axis and for the case of the molybdenum oxide, the better crystal direction is along the c axis.

Contacts should also have the same dimension in order to prevent asymmetries in *I-V* plots and annealing in vacuum is also very important in order to prevent poor contact quality and hysteresis behavior.

It was found that relation between the annealing temperature and the conductivity of molybdenum trioxide flakes is linear and it returns an ohmic behavior.

Also, it was discovered that after annealing the molybdenum samples, in an inert atmosphere, they have a recovery time of some hours until they become insulators again, with or without contacts made. The production of oxygen vacancies during annealing and their annihilation during prolonged exposure to air may explain these findings.

This kind of behavior was not detected for the gallium oxide samples for the temperatures used (from 170 to 300 degrees Celsius).

The reason for this different behaviors from two oxide semiconductors might be due to the temperatures at which this crystals were grown: gallium oxide was grown about 1500 °C and molybdenum trioxide were grown around 800 °C.

Following the common PPC models in literature for oxide semiconductors such as zinc oxide, it was proven that gallium oxide and molybdenum oxide go by the same be-

havior and an increase in current in a persistent way was observed when excited with ultraviolet light.

The PPC was attributed to oxygen molecules adsorbed at its surface that promoted confinement of the electrons in the conduction band. Ultraviolet light excites electrons from the valence band to the conduction band, allowing the correspondent holes to recombine with the electrons confined by the molecular oxygen. The remaining conduction electrons are therefore allowed to move freely and recombination with holes in the valence band is strongly reduced.

It was verified that the decay and rise curves of the current during irradiation studies could be described by the Kohlrausch stretched exponential function for all samples. Since the *I(V)-t* curves showed an exponential behavior a first order system approximation was done in order to determine the time constant for rise and decay curves.

Values of the γ parameter were fitted for each curve in order to understand and quantify the amount of different energy states contributing to the PPC phenomena in order to understand the impact of the in-situ studies of proton irradiation in the material, by means of the electrical response of the devices.

It was observed that gallium oxide emitted blue light when irradiated with protons in the same way it emitted when excited with UV light and for both gallium oxide and molybdenum trioxide they showed a persistent current when being irradiated.

It was also observed that the gallium oxide samples stop emitting after a few hours of being bombarded with the proton beam.

The dimension of the samples highly influence the response of an electronic device to irradiation. On one hand, the higher response of nanowires and nanoplates can simply be due to the fact that the entire structure is being totally pierced by the proton beam, while only part of the thick samples are reached by the proton beam. On the other hand, it is reasonable to assume that the higher surface to volume of the nanostructures will influence the conductivity through surface effects caused by higher concentration of adsorbed molecules.

In terms of sensor, nanoscale devices are more sensitive to the presence of radiation, but are more easily damaged than bulk samples or flakes with micrometers of thickness.

A brief protocol is presented so that, in the future, optimized procedures can be followed:

- When performing *I(V)-t*, *I-V*, etc. measurements always use the same electrode for the same contact in order to allow to evaluate the quality of contacts and to follow always the same conditions when performing UV and Proton Irradiation Studies;
- Always complement *I-V* with *I(V)-t* plots for the same experiment;
- Realize UV and Proton tests in the same conditions (same pressure) whether being in vacuum or in air so a good comparison can be achieved;
- Evaluate the UV response in the presence of different concentrations of oxygen and other gases;
- Do UV tests before and after irradiation process;
- Evaluate the recovery time of the sample, if that is relevant;
- For each *I(V)-t* curve always let the curve stabilize until it reaches at least 5 τ so a good mathematical treatment can be done;
- Test the influence of contacts and substrate during the UV and irradiation processes;
- Evaluate the devices sensitivity limits to radiation in order to quantify the capacity of the semiconductors as radiation sensors.

A personal future perspective would be the quantification of exfoliated samples in order to demonstrate the 2D configuration of the semiconductors in study. Some results were managed, but not in its total amplitude. Also, compare and try to model an approximation of density of states quantification regarding traditional contacts and compare with scanning tunneling spectroscopy. Once again, some results were calculated, but a more detailed approximation is needed.

Also, doping MoO_3 to become a p-type semiconductor and build a device using gallium oxide as a light emitter would be a great personal achievement.

References

[1] R. Ludeke, *Handbook of Surface Science, Vol.2, Chapter 11*, First. North-Holland, 2000.

[2] K. Lorenz, U. Wahl, E. Alves, E. Nogales, S. Dalmasso, and R. W. Martin, "High temperature annealing of rare earth implanted GaN films : Structural and optical properties," *Elsevier*, vol. 28, pp. 750–758, 2006.

[3] A. J. Chiquito, C. a Amorim, O. M. Berengue, L. S. Araujo, E. P. Bernardo, and E. R. Leite, "Back-to-back Schottky diodes: the generalization of the diode theory in analysis and extraction of electrical parameters of nanodevices," *J. Phys. Condens. Matter*, vol. 24, no. 22, p. 225303, 2012.

[4] Agilent Technologies, "Agilent B1500A Semiconductor Device Analyzer: User's Guide," p. 202, 2013.

[5] K. Lorenz, M. Peres, M. Felizardo, J. G. Correia, L. C. Alves, E. Alves, I. López, E. Nogales, B. Méndez, J. Piqueras, M. B. Barbosa, J. P. Araújo, J. N. Gonçalves, J. Rodrigues, L. Rino, T. Monteiro, E. G. Villora, and K. Shimamura, "Doping of Ga 2 O 3 bulk crystals and NWs by ion implantation," *SPIE*, vol. 8987, p. 89870M, Mar. 2014.

[6] J. C. Moore and C. V. Thompson, "A phenomenological model for the photocurrent transient relaxation observed in ZnO-based photodetector devices.," *Sensors (Basel).*, vol. 13, no. 8, pp. 9921–9940, 2013.

[7] A. Johannes, R. Niepelt, M. Gnauck, and C. Ronning, "Persistent ion beam induced conductivity in zinc oxide nanowires," *Appl. Phys. Lett.*, vol. 99, no. 25, p. 252105, 2011.

[8] H. Hosono, "Recent progress in transparent oxide semiconductors: Materials and device application," *Thin Solid Films*, vol. 515, no. 15 SPEC. ISS., pp. 6000–6014, 2007.

[9] R. P. Feynman, "Forces in Molecules," *Phys. Rev.*, vol. 56, no. (1939). Phys. Rev. 56, 340–343, 1939.

[10] "Physics Nobel Prize 2010.", http://www.nobelprize.org/nobel_prizes/physics/laureates/2010, visited on September 14th 2015.

[11] S. Y. Chou, Y. Liu, W. Khalil, T. Y. Hsiang, and S. Alexandrou, "Ultrafast nanoscale metal-semiconductor-metal photodetectors on bulk and low-temperature grown GaAs," *Appl. Phys. Lett.*, vol. 61, no. 7, pp. 819–821, 1992.

[12] T. C. Lovejoy, E. N. Yitamben, N. Shamir, J. Morales, E. G. Villora, K. Shimamura, S. Zheng, F. S. Ohuchi, and M. a Olmstead, "Surface morphology and electronic structure of bulk single crystal β-Ga2O3(100)," *Appl. Phys. Lett.*, vol. 94, no. 8, p. 081906, 2009.

[13] M. Blanco, M. Sahariah, H. Jiang, A. Costales, and R. Pandey, "Energetics and migration of point defects in Ga2O3," *Phys. Rev. B*, vol. 72, no. 18, p. 184103,. 2005.

[14] E. G. Víllora, S. Arjoca, K. Shimamura, D. Inomata, and K. Aoki, "β-Ga 2 O 3 and single-crystal phosphors for high-brightness white LEDs and LDs, and β-Ga 2 O 3 potential for next generation of power devices," *SPIE Photonics West 2014-OPTO Optoelectron. Devices Mater.*, vol. 8987, p. 89871U, 2014.

[15] "Characterization of Ga2O3 Single Crystal and Thin Film." http://www.int.washington.edu/REU/2012/students/hommerding_paper.pdf, visited on September 14th 2015.

[16] E. G. Víllora, K. Shimamura, Y. Yoshikawa, K. Aoki, and N. Ichinose, "Large-size β-Ga2O3 single crystals and wafers," *J. Cryst. Growth*, vol. 270, no. 3–4, pp. 420–426, Oct. 2004.

[17] A. Lüdge, H. Riemann, M. Wunscher, G. Behr, W. Löser, A. Mulznieks, and A. Cröll, "Floating Zone Crystal Growth," *Crystal Growth Processes Based on Capillarity: Czochralski, Floating Zone, Shaping and Crucible Techniques*, 2010.

[18] I. López, E. Nogales, B. Méndez, J. Piqueras, A. Peche, J. Ramírez-Castellanos, and J. M. González-Calbet, "Influence of Sn and Cr Doping on Morphology and Luminescence of Thermally Grown Ga $_2$ O $_3$ Nanowires," *J. Phys. Chem. C*, vol. 117, no. 6, pp. 3036–3045, 2013.

[19] et. al. Vila, M., "Intense luminescence emission from rare-earth-doped MoO 3 nanoplates and lamellar crystals for optoelectronic," *J. Phys. D. Appl. Phys.*, vol. 355105, no. 35, p. 355105, 2014.

[20] T. He and J. Yao, "Photochromism of molybdenum oxide," *J. Photochem. Photobiol. C Photochem. Rev.*, vol. 4, no. 2, pp. 125–143, 2003.

[21] M. V. Santos, "Sıntesis, propiedades fısicas y dopado de micro- y nanoestructuras de Bi2O3 y MoO3," Doctoral Thesis, Universidad Complutense de Madrid, Madrid, 2014.

[22] J. Budnar, M., Calmpbell, "Instrumentation for PIXE and RBS," *IAEA*, no. 1011–4289, 2000.

[23] M. Mayer, "Rutherford backscattering spectrometry (RBS)," *Garching Acad. Press. EURATOM Assoc.*, pp. 19–30, 2003.

[24] "Annealsys As-One." http://www.annealsys.com/docs/ASOne_EN_AS0300B22-04-04-14-43.pdf, visited September 14th 2015.

[25] M. E. Lin, Z. Ma, F. Y. Huang, Z. F. Fan, L. H. Allen, and H. Morkoç, "Low resistance ohmic contacts on wide band-gap GaN," *Appl. Phys. Lett.*, vol. 64, no. 8, pp. 1003–1005, 1994.

[26] "hamamatsu." http://www.hamamatsu.com/jp/en/L10290.html, visited September 14th 2015.

[27] J. Meyer, a. Shu, M. Kröger, and a. Kahn, "Effect of contamination on the electronic structure and hole-injection properties of MoO3 /organic semiconductor interfaces," *Appl. Phys. Lett.*, vol. 96, no. 13, 2010.

[28] Z. Zhang, K. Yao, Y. Liu, C. Jin, X. Liang, Q. Chen, and L.-M. Peng, "Quantitative Analysis of Current–Voltage Characteristics of Semiconducting Nanowires: Decoupling of Contact Effects," *Adv. Funct. Mater.*, vol. 17, no. 14, pp. 2478–2489, 2007.

[29] E. F. Hartman, T. a Zarick, T. J. Sheridan, E. F. Preston, and T. a Stringer, "Measurements of Prompt Radiation Induced Conductivity of Kapton," *Sandia Natl. Lab.*, vol. 7284, no. October, 2010.

[30] D. V Ahire, S. D. Shinde, G. E. Patil, K. K. Thakur, V. B. Gaikwad, V. G. Wagh, G. H. Jain, and V. N. N. Arts, "Preparation of MoO3 Thin Films By Spray Pyrolysis And Its Gas Sensing Performance," *Int. J. Smart Sens. Intell. Syst.*, vol. 5, no. 3, pp. 592–605, 2012.

[31] R. Ott, "Thermal and electrical resistance of metal contacts," Doctoral Thesis, Portland State University, Paper 325, 1967.

[32] "Semiconductor Detectors and Principles of Radiation-matter Interaction," *J. Appl. Sci.*, vol. 10, no. ISSN 1812–5654, pp. 3141–3155, 2010.

[33] http://www.srim.org/SRIM/SRIMPICS/STOPPLOTS.htm, visited September 14th 2015..

[34] C. Borschel and C. Ronning, "Ion beam irradiation of nanostructures – A 3D Monte Carlo simulation code," *Nucl. Instruments Methods Phys. Res. Sect. B Beam Interact. with Mater. Atoms*, vol. 269, no. 19, pp. 2133–2138, 2011.

[35] L. Binet and D. Gourier, "ORIGIN OF THE BLUE LUMINESCENCE OF β-Ga2O3," *J. Phys. Chem. Solids*, vol. 59, no. 8, pp. 1241–1249, 1998.

[36] J. C. Gillespie, "Measurement of The Temperature Dependence of Radiation Induced Conductivity in Polymeric Dielectrics," UtahState Univerity, 2013.

[37] U. Rau, M. Schmitt, J. Parisi, W. Riedl, and F. Karg, "Persistent photoconductivity in Cu(In,Ga)Se2 heterojunctions and thin films prepared by sequential deposition," *Appl. Phys. Lett.*, vol. 73, no. 2, pp. 223–225, 1998.

[38] B. Claflin, D. C. Look, S. J. Park, and G. Cantwell, "Persistent n-type photoconductivity in p-type ZnO," *J. Cryst. Growth*, vol. 287, no. 1, pp. 16–22, 2006.

[39] J. Bao, I. Shalish, Z. Su, R. Gurwitz, F. Capasso, X. Wang, and Z. Ren, "Photoinduced oxygen release and persistent photoconductivity in ZnO

nanowires.," *Nanoscale Res. Lett.*, vol. 6, no. 1, p. 404, 2011.

[40] M. R. Alenezi, S. J. Henley, and S. R. P. Silva, "On-chip Fabrication of High Performance Nanostructured ZnO UV Detectors," *Sci. Rep.*, vol. 5, p. 8516, 2015.

[41] Y. Li, F. Della Valle, M. Simonnet, I. Yamada, and J.-J. Delaunay, "Competitive surface effects of oxygen and water on UV photoresponse of ZnO nanowires," *Appl. Phys. Lett.*, vol. 94, no. 2, p. 023110, 2009.

[42] A. Omar, M., *Solid State Physics*. Addison, Wesley, 1993.

[43] M. N. Berberan-Santos, E. N. Bodunov, and B. Valeur, "Mathematical functions for the analysis of luminescence decays with underlying distributions 1. Kohlrausch decay function (stretched exponential)," *Chem. Phys.*, vol. 315, no. 1–2, pp. 171–182, 2005.

[44] M. Boens, N; Van der Auweraer, "Identifiability of models for time-resolved fluorescence with underlying distributions of rate constants." *Photochem Photobiol Sci*, vol. 13(2), pp. 422–30, 2014.

[45] J. Reemts and A. Kittel, "Persistent photoconductivity in highly porous ZnO films," *J. Appl. Phys.*, vol. 101, no. 1, pp. 1–6, 2007.

[46] W. Bolton, *Mechatronics, Electronic Control Systems In Mechanical and Electrical Engineering.pdf*, Third Edit. Pearson Prentice Hall, 2003.

[47] http://www.srim.org/SRIM/SRIMPICS/STOP01/STOP0131.gif, visited September 14th 2015.

[48] http://www.srim.org/SRIM/SRIMPICS/STOP01/STOP0142.gif, visited September 14th 2015.